

Computational Fluid Dynamics Modeling of Flow in Fuel Cell Channels

by
Martin William Bowers

B.Eng. University of Victoria, 1995

A Thesis Submitted in Partial Fulfillment of the

Requirements for the Degree of


MASTER OF APPLIED SCIENCE

in the Department of Mechanical Engineering

We accept this thesis as conforming to the required standard



Dr. N. Djilali, Supervisor (Department of Mechanical Engineering)



Dr. G. McLean, Departmental Member (Department of Mechanical Engineering)



Dr. D. S. Scott, Departmental Member (Department of Mechanical Engineering)



Dr. M. van Emden, External Examiner (Department of Computer Science)

© Martin William Bowers, 1997

University of Victoria

All rights reserved. This thesis may not be reproduced in whole or in part, by photocopying or other means, without the permission of the author.

QA911
B59

Abstract

Proton Exchange Membrane (PEM) Fuel Cells present an opportunity for highly efficient and low emission power generation for transportation purposes. The PEM fuel cell features the more environmentally compatible fuel source of hydrogen as well as a comparatively low operating temperature of around 80° Celcius. With these fundamental advantages, the PEM fuel cell is poised to become a major factor in worldwide transportation applications. A fundamental understanding of many of the transport process that occur in a fuel cell has yet to be developed.


This thesis presents a computational fluid dynamics (CFD) study of flow in fuel cell channels undertaken to provide understanding of the basic hydrodynamic processes behind the operation of fuel cells. The model was also desirable for the purpose of providing design information for new fuel cells. The model is based on the numerical solution, using a commercial CFD code: CFX-4.1, of the full Navier Stokes equations coupled with chemical concentration transport equations.

The model is validated for simplified conditions for which data is available in the literature. The final model developed in this thesis features a three dimensional duct with an attached porous section and accounts for the slip velocity at the

interface, which is found to be an important factor in the determination of the flow field.

The most important factor determining the flow solution is the permeability of the porous section. The pressure drop across the porous section causes a uniform suction velocity distribution through the porous section. This suction velocity creates a distribution layer within the duct above the porous section that initiates the uniform velocity within the porous section. The maximum mass transport ability of the duct was modeled utilizing a diffusive boundary condition at the catalyst layer interface. The results indicate that the convective transport abilities of the duct do not limit the supply of reactant and hence do not limit the operation of the fuel cell.

Examiners:




Dr. N. Djilali, Supervisor (Department of Mechanical Engineering)



Dr. G. McLean, Departmental Member (Department of Mechanical Engineering)



Dr. D. S. Scott, Departmental Member (Department of Mechanical Engineering)



Dr. M. van Emden, External Examiner (Department of Computer Science)

Acknowledgements

I would like to thank my supervisor, Ned Djilali, for his help with all aspects of my degree. I would also like to thank NSERC, the University of Victoria, and the Advanced Systems Institute for funding my research. Furthermore I appreciated the contribution of BG plc in the form of additional funding for the NGFT project. Finally, I would to thank all the members of the NGFT research group for creating an enjoyable and intellectually stimulating research environment.

Table of Contents

ABSTRACT.....	II
ACKNOWLEDGEMENTS.....	IV
TABLE OF CONTENTS	V
LIST OF FIGURES	XI
LIST OF TABLES.....	XV
NOMENCLATURE	XVI
CHAPTER 1 INTRODUCTION.....	1
1.1 Introduction to Fuel Cells	1
1.2 Need For Research.....	2
1.2.1 Membrane Model.....	3
1.2.2 Tube Cell Project	4
1.3 Existing Work.....	5
1.3.1 Single Component Impermeable Wall Results	5
1.3.2 Porous Walls	5
1.3.3 Experimental Results.....	6
1.4 Two Phase Flow.....	7
1.4.1 Multi-component Flow.....	7

1.5 Goals of The Research	8
1.5.1 Verification of Previous Numerical Models.....	9
1.5.2 Input to the MEA model	9
1.5.3 Flow Patterns.....	9
1.5.4 Concentration Distributions of Chemicals	10
1.5.5 Determination of Optimum Channel Cross-Sections	10
1.6 Research Methodology	10
1.6.1 Navier Stokes Equations.....	11
1.6.1.1 Numerically Solving the Navier Stokes Equations	13
1.6.2 Step One - Grid Refinement	13
1.6.2.1 General Description of Grid Refinement.....	14
1.6.2.2 Grid Refinement for this Thesis	15
1.6.2.3 Geometric Grid Refinement	16
1.6.2.4 Example: Square Cross-Section Refinement.....	17
1.6.2.5 Cost of Grid Refinement.....	17
1.6.3 Step Two - Differencing Scheme	18
1.6.4 Porous Sections.....	19
1.6.5 Multi Component Flow	20
1.6.6 Integration with the MEA model.....	21
1.7 Porous Materials	21
1.7.1 Porous Properties	21
1.7.1.1 Porosity	22
1.7.1.2 Permeability	22

1.7.2 Isotropy.....	23
1.7.3 D'Arcy Flow.....	23
1.7.4 Navier Stokes Equations in Porous Materials.....	24
1.8 Physical Properties Considered.....	26
CHAPTER 2 - VALIDATION WORK	28
2.1 Impermeable Wall Validation Work.....	28
2.1.1 Triangular Duct.....	28
2.1.2 Grid for Triangular Results.....	29
2.2 Results.....	30
2.2.1 Grid Refinement and Shear Force.....	30
2.2.2 Heat Transfer.....	31
2.2.2.1 Nusselt Number.....	31
2.2.2.2 Differencing Schemes.....	33
2.2.2.3 Hybrid Differencing Scheme.....	33
2.2.2.4 QUICK Scheme.....	35
2.2.2.5 The CCCT Scheme.....	36
2.2.3 Differencing Results.....	37
2.2.4 Grid Refinement Results.....	38
2.3 Permeable Wall Validation.....	38
2.3.1 The Berman Solution.....	38
2.3.2 Comparison with the Berman Solution.....	40
CHAPTER 3 ADDING A POROUS SECTION.....	43

3.1 Need for a Porous Section	43
3.2 Definition of a Porous Interface.....	43
3.3 Integrating α into the fluid dynamics	45
3.3.1 <i>The Beavers and Joseph Solution</i>	47
3.3.2 <i>The Saffman Solution</i>	49
3.3.3 <i>The Exact 2-D solution</i>	50
3.4 Porous Section Boundary Conditions	52
3.4.1 <i>Velocity Boundary Condition</i>	52
3.4.2 <i>Heat Transfer</i>	53
3.5 The Porous Section Model.....	54
3.6 Porous Section Grid.....	54
3.7 Slip Velocity Results	55
3.7.1 <i>Implementation of the Vafai Slip velocity</i>	55
3.7.2 <i>Grid Resolution</i>	56
3.8 Convergence within Porous Sections - Double Precision Variables.....	59
3.8.1 <i>Additional benefits of Double Precision Variables</i>	60
CHAPTER 4 SINGLE COMPONENT RESULTS	61
4.1 Two Dimensional Results.....	62
4.1.1 <i>Domain Considered</i>	62
4.1.2 <i>Grid Used</i>	62
4.2 Parametric Results.....	63
4.2.1 <i>Pressure Drop</i>	63

4.2.2 Entrance Effects	64
4.2.3 Friction Factor	64
4.2.4 Injection Results	66
4.2.5 Suction Results	67
4.2.6 Entrance Length	68
4.3 Three Dimensional Results	69
4.3.1 Domain Considered	69
4.3.2 Grid Used	70
4.3.3 Injection Results	71
4.3.4 Suction Results	73
CHAPTER 5 MULTI COMPONENT MODEL	75
5.1 Mass Fraction Equation	75
5.2 Modification Details	75
5.2.1 Mass Fraction Boundary Conditions	76
5.2.2 Sources and Sinks	76
5.2.3 A Natural Mass Fraction Boundary Condition	77
5.2.4 Sink Options	78
5.2.4.1 Verification of Sink Term	79
5.2.4.2 Balance of Oxygen Mass Flow	81
5.2.5 Maximum Diffusion Boundary Condition	81
5.2.6 Pressure Boundary Condition	83
5.3 Grid Used	84

5.4 Three Dimensional Results	84
5.4.1 Concentration Profiles	85
5.4.2 Oxygen Velocity at the Catalyst Velocity.....	86
5.4.3 Velocity Contours.....	88
5.4.4 Pressure Profiles	91
5.4.5 U Velocity Development	94
5.5 Resistance Effects	95
6.0 CONCLUSIONS	98
6.1 Limitations of the Model and Recommendations	100
6.1.1 Compressibility.....	100
6.1.2 Permeability	101
6.1.3 Mass Transport Capability.....	101
6.1.4 Multi-Component Flow.....	102
6.1.5 Multi-Phase Flow	102
BIBLIOGRAPHY.....	103

List Of Figures

Figure 1.1 Internal Geometry of a PEM Fuel Cell	2
Figure 1.2: Possible Tube Cell Configurations	4
Figure 1.3: Channel Co-ordinate System.....	15
Figure 1.4: Example of Square Section Refinement. The left square has 4 grid points, and the right square has 10. Both have a geometric ratio of 1.3.....	17
Figure 1.5: Cross-Section of Porous Section model	19
Figure 2.1: Domain considered for the triangular duct.	28
Figure 2.2: Grid for Triangular Duct. Note symmetry boundaries on the short.....	29
sides of the quadrilateral	29
Figure 2.3: Grid Refinement Effects on Shear Force at the Solid Walls for an Impermeable Triangular Duct. The published data is from Kakac et al [2]	30
Figure 2.4: Computational Stencil for Evaluating Fluxes under Various Differencing Schemes.	33

Figure 2.5: Grid Refinement and Differencing Scheme Effects on Heat Transfer. The Nusselt number is based on a constant heat flux.....	37
Figure 2.6: Illustration of the parallel plates considered by Berman	39
Figure 2.7: U Velocity Comparison between permeable wall model and the Berman solution.....	40
Figure 2.8: V Velocity Comparison between permeable wall model and the Berman solution.....	41
Figure 3.1: Detailed View of the Surface of a Porous Material	44
Figure 3.2: Illustration of Velocity Distribution Inside a Porous Section and into the Surrounding Channel.....	46
Figure 3.3: Porous Section Model	54
Figure 3.4: Slip Velocity Comparison between present model and CFX default.....	55
Figure 3.5: Coarse Grid in X and Y directions for Coupled Porous Section	57
Figure 3.6: Fine Grid in X and Y directions for Coupled Porous Section	57
Figure 3.7: Effect of Grid Refinement on Near Interface Velocity.....	58
Figure 4.1: Domain Considered for 2D Simulations	62

Figure 4.2: Friction Factor Results for 2D Case with Injection. The Reynolds number is 1000, and Re_w is the wall Reynolds number.....	66
Figure 4.3: Friction Factor Results for 2D Case with Suction	67
Figure 4.4: Domain Considered for Three Dimensional Square Duct.....	69
Figure 4.5: Three dimensional square grid viewed from the X direction.....	70
Figure 4.6: Three Dimensional Friction Factors: Injection.....	72
Figure 4.7: Friction Factors for Three Dimensional Case with Suction.....	73
Figure 5.1: Upwind Boundary conditions at the porous section.....	77
Figure 5.2 Comparison of oxygen profiles under CFX default and with modified sink term. The concentration has been non-dimensionalized by the inlet concentration of 0.2.....	80
Figure 5.3: Illustration of Diffusion from the bottom of the electrode to the Catalyst layer.....	82
Figure 5.4: Oxygen concentration Profiles at $X = 25$. Concentration is non-dimensionalized by the inlet concentration of 0.2.....	85
Figure 5.5: Plot of Oxygen Velocity (\propto Current Density) along the X Axis of the duct. The velocities are averaged in the Z direction.	87

- Figure 5.6: W and V Velocity contours at the X plane = 25. The constant V velocity inside the porous section has been shaded in for visibility..... 88**
- Figure 5.7: Contours of W velocity at the porous interface. The contours in the inlet region have been clipped to provide resolution over the remainder of the duct. 90**
- Figure 5.8: Pressure Distribution across the duct. Pressure is non-dimensionalized by one atmosphere. 92**
- Figure 5.9: Pressure Distribution for the Maximum Diffusion Case..... 93**
- Figure 5.10: Centreline U Velocity Along the Duct. Velocity is non-dimensionalized by the inlet mean velocity. 94**
- Figure 5.11: V Velocity at the Catalyst Layer along Square Duct Axis for Different Porous Section Resistances. The Catalyst Boundary Condition is constant pressure of -4 atmospheres with respect to inlet pressure. 96**

List of Tables

TABLE 1.1: PHYSICAL PROPERTIES AND THEIR VALUES	26
TABLE 2.1 APPROXIMATION OF FACE VALUE FOR VARIOUS DIFFERENCING SCHEMES. A UNIFORM GRID IS ASSUMED FOR CENTRAL DIFFERENCING.	34
TABLE 3.1: COMPUTATIONAL TIME COMPARISON BETWEEN SINGLE PRECISION AND DOUBLE PRECISION VARIABLES. THE CASE CONSIDERED WAS A 2D SINGLE COMPONENT CASE WITH MODIFIED SLIP VELOCITY AND $REW = 0.001$	60
TABLE 4.1: GRID PARAMETERS IN THE Y DIRECTION FOR THE TWO DIMENSIONAL SINGLE COMPONENT MODEL.....	63
TABLE 4.2: GRID SUMMARY IN THE Y AND Z DIRECTIONS FOR THE THREE DIMENSIONAL SINGLE COMPONENT MODEL.....	71
TABLE 5.1 OXYGEN MASS FLOW BALANCE.....	81
TABLE 5.2 VARIOUS ELECTRODE PERMEABILITIES USED IN MODELS ...	97

Nomenclature

[]	Concentration or mass fraction (ND)
A	Inertia Parameter in porous material (ND)
a	Cross Sectional Area of Duct (m^2)
B	Resistance Parameter (ND)
Cf	Friction Factor (ND) $Cf = \frac{(\tau_t + \tau_b)D_h}{\mu u}$
D	Diameter (m)
Da _H	D'Arcy Number $Da_H = \frac{k}{H^2}$
D _h	Hydraulic diameter $D_h = \frac{4A}{P}$ (m)
D _i	Diffusion Coefficient (m^2/s)
G	mass flux vector
h	Half height of channel (m)
L _e	Non-dimensional Entrance Length $L_e = \frac{L}{D_h}$
K	Thermal conductivity of fluid ($W/m^2 K$)
k	Resistance of porous material (m^2)
Nu	Nusselt Number $Nu = \frac{q_w L}{k \Delta T}$
O()	Order of magnitude
P	Perimeter of cross section (m)
p	Pressure (Pa)
Q	D'Arcy flow rate (m^3/s)
q	Heat flux (W/m^2)
R	Resistance of porous material $R = \frac{\mu}{k}$

Re	Reynolds Number $Re = \frac{\rho U D_h}{\mu}$
Rep	Pore Reynolds Number $Re_p = \frac{\rho Q k^{1/2}}{\mu}$
Rew	Wall Reynolds Number $Re_w = \frac{\rho V_w D_h}{\mu}$
Sc	Schmidt Number $Sc = \frac{\mu}{\rho D_i}$
T	Temperature (K)
U	Bulk velocity (m/s)
U _i	Interface velocity (m/s)
u	Local x velocity
u _s	Slip Velocity (m/s)
v	Local y velocity
V _w	Wall Velocity (m/s)
w	Local z velocity
X	Position along duct main flow axis
Y	Position normal to the porous wall
Z	Position parallel to porous wall and normal to flow direction

Greek Symbols

α	Slip Parameter (ND)
β	Slip Parameter (m^{-1})
τ	Shear stress (Pa)
μ	Dynamic viscosity (Pa s)
σ	Channel height to pore size ratio (ND) $\sigma = \frac{h}{\sqrt{k}}$
θ	Non-dimensional temperature $\theta = \frac{T}{T_{avg}}$
ρ	Volumetric density of fluid (kg/m^3)
λ	Non-dimensional y distance $\lambda = \frac{y}{h}$

Chapter 1 Introduction

1.1 Introduction to Fuel Cells

A fuel cell is an electro-chemical device that is used to produce electrical energy from chemical potential energy. The first fuel cell was invented by Grove in 1837. Fuel cell technology is hindered by complex electrochemistry and was eclipsed by the combustion engine, which arrived after the first fuel cell. Fuel cells have the intrinsic advantage, however, of not requiring a high temperature heat reservoir and hence have their efficiency determined only by the chemical potential available at their operating temperature. A typical fuel cell operates using oxygen as the oxidant and a hydrocarbon based fuel such as methanol or hydrogen reformed from a hydrocarbon. The Proton Exchange Membrane (PEM) Fuel cell uses a solid hydrated polymer membrane that carries protons from the hydrogen side to the oxygen side where water is produced. The membrane itself requires hydration with water before use. The active process of transporting the protons moves liquid water through the membrane which must be replaced by adding water to the reactant streams. The state of the art technology is represented by the Ballard PEM fuel cell of which a schematic is shown below. The flow channels are machined from solid plates.

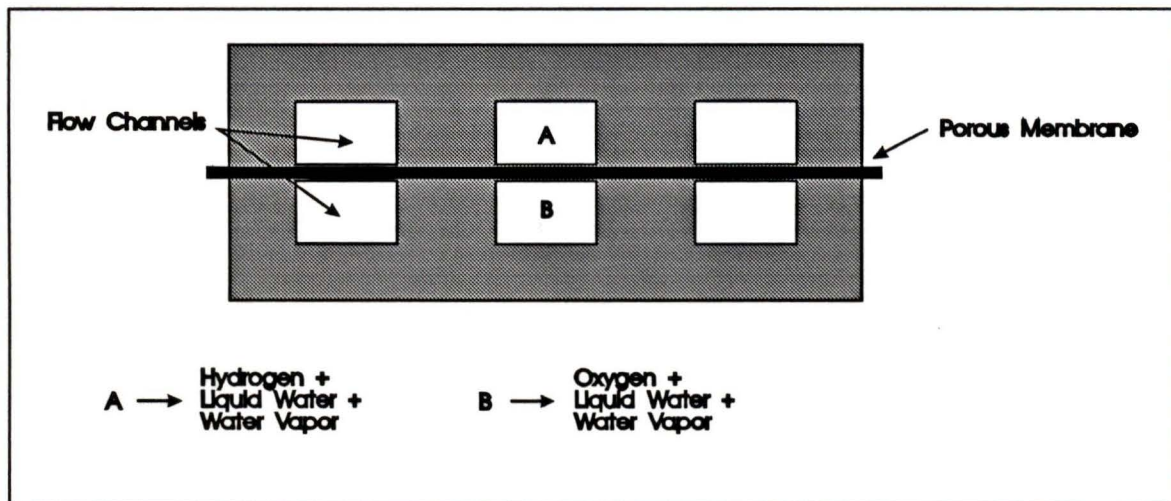


Figure 1.1 Internal Geometry of a PEM Fuel Cell

The flow channels carry the reactants to the sides of the electrochemical assembly where the chemical reactions take place. The complete reaction takes place in a PEM cell at the membrane and electrode interface on the oxygen (cathode) side. While a fuel cell theoretically has a very high efficiency (on the order of 95%), actual efficiencies of around 50% are achieved in practice. Therefore 50% of the chemical potential energy is converted into thermal energy. This thermal energy must be removed in order to maintain an efficient steady state operation. The flow channels inside the fuel cell are also responsible for removing a significant part of the excess heat from the fuel cell.

1.2 Need For Research

The flow inside a fuel cell is crucial to the operation of the fuel cell. The channels transport both the reactant laden inlet stream to the membrane, they

also transport away the waste products. An understanding of the velocity distributions and the influencing factors on the flow inside the channels is necessary if the optimal shape and configuration of porous layers for a flow channel is to be determined in a systematic fashion. The flow inside the tubes is complex and features two phase and multi component flow combined with porous media, heat transfer and phase changes. The only simple aspect to the flow is that it is laminar under the current technology. In order to begin to understand the behaviour of this flow and how it responds to changes in geometry and materials, an extensive battery of tests would have to be conducted to cover all possible flow configurations. Even with dimensional analysis, there are still many factors to be considered. Computational fluid dynamics offers an alternative method that allows a good understanding of the flow and reduces the number of experimental tests that need to be performed.

1.2.1 Membrane Model

A concurrent research project within the NGFT project is a numerical investigation of the behaviour of the electrochemical assembly [1]. This project should lead to a better understanding of the flow within the chemically reacting region of the fuel cell. This project requires boundary conditions involving pressure, temperature, and chemical species, which can only be provided by the physical conditions in the channel outside the electrodes. In the same manner the electrochemical assembly impacts the flow channels by changing the heat

transfer, chemical species present and phases of species present. The two projects complement each other to provide a complete model of the internal behaviour of a fuel cell.

1.2.2 Tube Cell Project

The tube cell project is a concurrent project that proposes to redesign the entire fuel cell system based on parallel tubes that are formed by a membrane surface and thin walls around the membrane as opposed to using a plate with an engraved channel. The tube cell offers the potential of greater power densities as well as more flexibility in design, manufacturing and operation than the flat plate design. In particular, the shape of the tubes has been freed from the constraint of a sinuous groove in a machined plate. Almost any geometric configuration is possible. Some cross-sections under consideration are shown below in Figure 1.2.

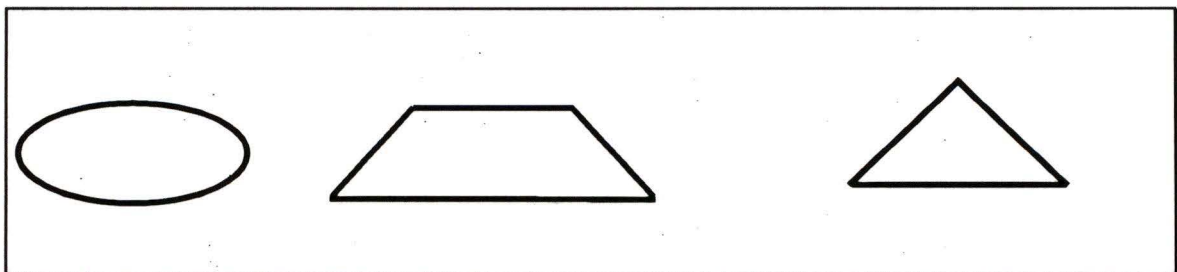


Figure 1.2: Possible Tube Cell Configurations

1.3 Existing Work

The complete problem of a reacting flow through a porous medium attached to a duct has never been investigated. Various attempts at modelling this problem with simplified models have been made. These models will be reviewed in order of complexity before the proposal of research in this area is presented.

1.3.1 Single Component Impermeable Wall Results

The flow patterns and heat transfer properties of a variety of different, impermeable walled ducts under laminar single phase flow have been investigated reasonably extensively. Kakac et al have summarised the results in [2]. The data still lacks some of the important aspects of the practical problem because entrance properties have not been investigated very thoroughly. While this work is useful for verifying the initial steps in generating the CFD model, the data does not provide sufficient accuracy to make detailed design choices, which are the goals of this research.

1.3.2 Porous Walls

Internal flow through ducts with porous walls has been important for applications in filtration and purification processes. Many chemical processes utilise a membrane or other porous material. Some progress has been made in understanding the effect of porosity on internal flow, but it is not yet well

developed. There have been several analytical studies such as Olson's one-dimensional study [3] and Berman's two-dimensional analysis [4]. Most of these attempts have focused on a closed form analytical solution, which requires a number of simplifying assumptions. The assumptions are reasonable, but only over a restricted range of parameters. A recent paper in 1994 by Hwang [5] extended the theoretical analysis to a square duct with one porous wall. They studied both injection and suction through the porous wall. This geometry is typical of the current PEM fuel cell configuration. For injection they found an increase in the pressure drop, and a decrease in the Nusselt number. The velocity distribution was also shifted to the side opposite to the porous wall. This was followed by an experimental investigation [6], which confirmed within experimental error the numerical results. Further details as well as a rectangular duct model are found in Cheng's Ph. D. dissertation [7].

1.3.3 Experimental Results

After the theoretical investigation, Cheng and Hwang [6] published an experimental investigation of the same square duct geometry. Air under laminar flow conditions was allowed to flow down the duct and additional air was injected through the porous wall. The friction factors and Nusselt numbers were measured and found to correspond well with the theoretical results obtained in the earlier study. In general there has been little published experimental work done on porous walled ducts. The work that is available in the literature typically

features either parallel plates or a uniformly porous circular duct. Neither configuration bears much resemblance to the geometry of a real fuel cell. Any work that does feature a more complicated geometry stems from problems encountered in chemical processes. These experiments feature turbulent flow since most chemical processes occur under turbulent conditions in order to improve the overall rate of all processes within the fluid.

1.4 Two Phase Flow

Two phase flow involves the flow of either a gas and a liquid, or two immiscible fluids such that the properties of the combined fluid are not simply an average of the global properties of each component. Two phase flow regimes exist within the fuel cell, but they are beyond the scope of this thesis. Two phase flows are extraordinarily complex and many "simple" problems are still not fully understood. The two phase flow within the fuel cell is further complicated by phase change, heat transfer, complex geometry and the effects of a porous medium.

1.4.1 Multi-component Flow

A simpler subset of multi-phase flow is multi-component flow. Multi-component flow refers to the consideration of multiple chemical species, which are of the same phase and are wholly miscible. In the case of a fuel cell, the air stream on

the cathode side features oxygen (O_2), nitrogen (N_2) and water vapour (H_2O (g)). The fuel stream contains hydrogen (H_2) and water vapour (H_2O (g)). The behaviour of a fluid that contains multiple components can be solved for with one set of momentum and continuity equations for the entire fluid. The behaviour of the individual components within that fluid can be solved for with scalar equations that are coupled to the Navier Stokes equations. One additional equation is required for each additional component in the flow. If the concentrations of each respective species remain constant, then the whole mixture can be treated as one fluid with appropriate physical properties. The oxygen, however, is depleted as the stream flows down the channel, and the water vapour content may vary with temperature. The corresponding physical properties, which affect the flow, are changed and hence the flow changes. Depending on the extent of the domain considered, the changes in physical properties may be significant. This effect is also important in the membrane model where the impact on the chemical processes is even more significant. The chemical processes in turn have an effect on heat transfer rates. Multi-component flow models are used by Lu and Djilali [8] to model the membrane and electrode assembly.

1.5 Goals of The Research

There are several goals of various natures which were the target of this research. They are discussed in the following sub-sections. The factor behind

all of the goals is that previously, only large-scale data on average properties of the flow in fuel cell channels was known. Attempts by Ballard at optimisation of overall fuel cell performance through flow channel variation have been limited to carefully considered experimental variations.

1.5.1 Verification of Previous Numerical Models

The research involved a considerably more complex numerical model which was compared with previous results to verify qualitative trends and to compare quantitative results.

1.5.2 Input to the MEA model

One of the primary needs and thus an important goal for this research was to produce heat and mass transfer coefficients at the channel / MEA model interface which would allow the MEA model to better simulate real operating conditions.

1.5.3 Flow Patterns

An investigation into the flow channels should lead to an understanding of the transport mechanisms that are important to the flow and those transport mechanisms which are negligible. To date there was no information on the flow

patterns or important features in the velocity distributions within the tubes. With detailed knowledge of the flow behaviour at a smaller scale level, it should be possible to guide the optimisation of the flow channels in the most fruitful direction.

1.5.4 Concentration Distributions of Chemicals

The concentration distributions are crucial to the reaction rates possible in the fuel cell. The research was expected to reveal information on the distribution of oxygen under various operating conditions.

1.5.5 Determination of Optimum Channel Cross-Sections

As a final goal, driven by the tube cell project, the flow channel modelling was used to determine what the optimum channel cross-sections would be. The information gained from the flow patterns and the concentration profiles could be used to determine the optimum cross-section.

1.6 Research Methodology

This project utilised the commercial computational fluid dynamics (CFD) program CFX-F3D. This program is a structured grid multi-block flow solving code. It is a state of the art industrial package, which in recent years has been applied to

many problems in various fields. It features a number of the best available models for specific applications (e.g. turbulence, two-phase flow and porous media) and provides a robust and reliable platform to customize and develop new models via the use of user written subroutines. The code handled a full three dimensional simulation of the flow channels. The complete Navier-Stokes equations, which describe the flow field, were solved without simplifying assumptions on the geometry. The only approximations were in the level of refinement in the computational grid.

1.6.1 Navier Stokes Equations

The Navier Stokes equations describe the behaviour of a Newtonian fluid. The complete set of equations is:

Continuity (Conservation of Mass)

$$\frac{\partial \rho}{\partial t} + \nabla \cdot (\rho \mathbf{U}) = 0 \quad (1)$$

Conservation of Momentum

$$\frac{\partial \rho \mathbf{U}}{\partial t} + (\rho \mathbf{U} \otimes \mathbf{U}) = \mathbf{B} + \nabla \cdot \underline{\underline{\sigma}} \quad (2)$$

where $\underline{\underline{\sigma}}$ is the stress tensor and

$$\underline{\underline{\sigma}} = -p \underline{\underline{\delta}} + \left(\xi - \frac{2}{3} \mu \right) \nabla \cdot \underline{\underline{\mathbf{U}}} \underline{\underline{\delta}} + \mu (\nabla \mathbf{U} + (\nabla \mathbf{U})^T) \quad (3)$$

In the equations, \mathbf{U} is the velocity vector, \mathbf{B} is the body force other than pressure, ρ is the density, ξ is the bulk viscosity, μ is the fluid viscosity, t is time, and p is the pressure.

In the cases considered for this thesis, the equations can be simplified to a steady state, constant property and incompressible version. The steady state simplification is made because the average flow properties are desired and not every detail in time. The incompressible simplification is made because velocities were not expected to reach 30 percent of the speed of sound, which is the standard threshold in fluid dynamics for transition from incompressible to compressible flow. Finally the properties of the fluids under consideration do not vary significantly over the temperatures and pressures under consideration. The simplified Navier Stokes equations are:

Simplified continuity

$$\nabla \cdot \mathbf{U} = 0 \quad (4)$$

Simplified conservation of momentum

$$\nabla \cdot (\rho \mathbf{U} \otimes \mathbf{U}) - \nabla \cdot (\mu (\nabla \mathbf{U} + (\nabla \mathbf{U})^T)) = -\nabla p \quad (5)$$

1.6.1.1 Numerically Solving the Navier Stokes Equations

The Navier-Stokes equations are non-linear and strongly coupled. Because they are so strongly coupled, an analytical solution to the equations exists for only the simplest geometry and boundary conditions. The flows considered by this thesis do not fall into the realm of possibilities with analytical solutions.

Therefore a numerical solution was required to solve the differential equations.

The method chosen was the finite-volume method because the finite volume method has been developed more than the finite element method, and no commercial CFD codes which utilize a finite-element approach and include porous material exist. The finite volume method employed in CFX uses a volumetric grid, referred to as simply the grid, to create the finite volumes over which the governing equations are solved numerically. The grid is defined by grid points, which are created through the combination of CFX user guidance and some minor automation provided by CFX.

1.6.2 Step One - Grid Refinement

Grid refinement is an essential step in assessing the accuracy of a numerical solution. Grid design and grid refinement can be considered more of an art, than a pure mathematical problem. Much work has been spent on grid design [9,10] but it remains a difficult problem to solve exactly and hence automation is rare. There are many commercial and custom CFD codes which utilize semi

automatic grid generation. In this method the user guides the grid, while the grid generation software does most of the raw calculation work behind grid design and refinement.

1.6.2.1 General Description of Grid Refinement

Grid refinement is a measure of the degree of resolution possible in the numerical solution. In the same manner as a filter, a finer grid is capable of resolving smaller aspects of the flow. It also will produce a more accurate solution compared to the true physical problem. It is always possible to refine the grid further and generate more accurate solutions, however, because of the large computational and memory requirements for solving the Navier-Stokes and associated concentration transport equations in three dimensions, it is highly desirable to develop a grid with the minimal number of computational nodes. The research involved using a known problem with either an analytical or a numerical solution and comparing various levels of grid refinement to see how many grid points are required to achieve a certain level of accuracy in the solution. Once known, the grid size for all further work was based on the known grid resolution required to achieve a solution within 5% of the analytical solution. This process was performed on several different problems to ensure that the results are generally representative of similar problems.

1.6.2.2 Grid Refinement for this Thesis

For the complete 3-D problem there are two directions of primary interest, while the third direction is less critical. The variations in the Y and Z directions are of local importance and hence must be resolved accurately, while the variations in the X direction are much less but are important over the length of the duct.

These directions are shown with respect to the duct in the following figure 1.3.

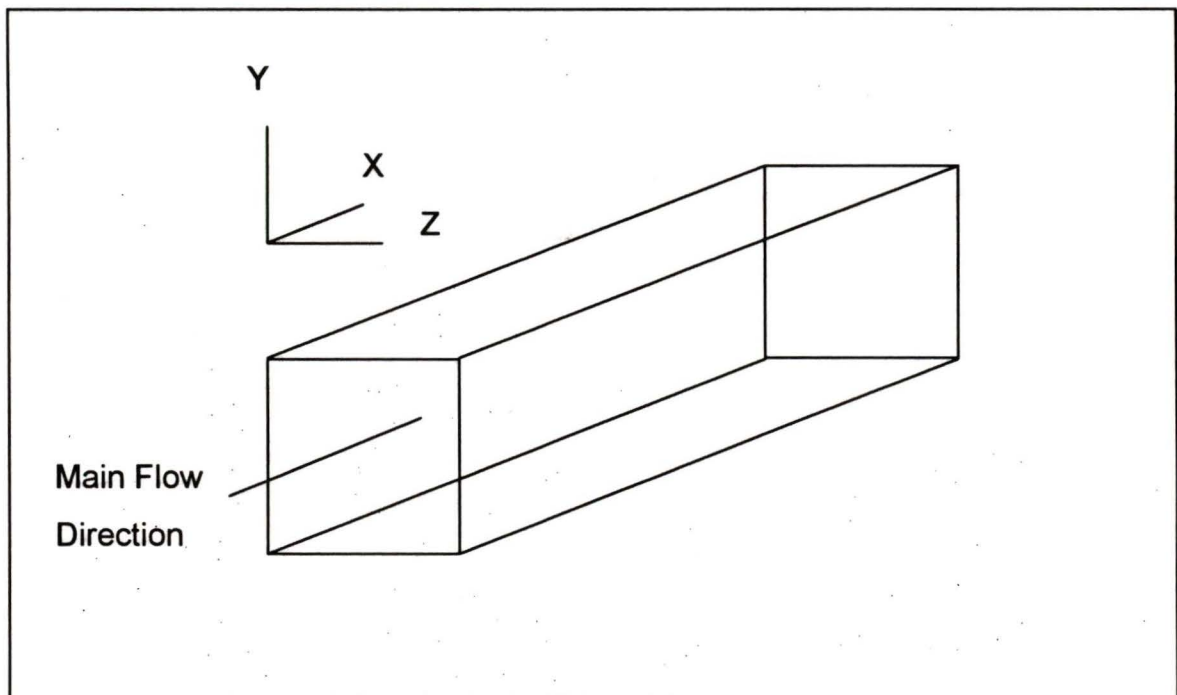


Figure 1.3: Channel Co-ordinate System

Therefore it is desirable to have a fine grid in the Y and Z directions, but it is acceptable to have a coarser grid in the X direction. This is not possible to the degree desired, because the numerical accuracy and solution procedure preclude extreme grid aspect ratios and hence the X direction necessitates a

finer grid than required purely for numerical resolution. Only a relatively short duct section can therefore be simulated. For grid refinement the grid resolution can be increased in either of the two dimensions of local interest, and it can also be preferentially increased in a region of particular interest.

1.6.2.3 Geometric Grid Refinement

An additional parameter than can be varied in the grid refinement in the geometric ratio between adjacent grid points. By using a geometric ratio in creating the grid, grid points can be clustered next to geometric features that have the greatest impact on the flow field. Alternatively grid points can be clustered in areas that have the largest gradients which also impact the flow field. Secondly, grid points can be clustered in regions of particular interest regardless of whether the flow field is heavily influenced by that area. As a general rule it is best to keep geometric ratios at 1.3 to maintain accuracy [11]. At higher geometric ratios, the important effects occurring in the smaller grid volume may not be carried into its neighboring and larger grid volume. For this thesis, the grid geometric ratio was made as large as possible in the Y direction, because values near the wall have the greatest effect. Fortuitously the values near the wall are also of the greatest interest because they govern the injection or suction velocity through the porous wall of the duct.

1.6.2.4 Example: Square Cross-Section Refinement

For a square cross-section, grid refinement would have the following effect:

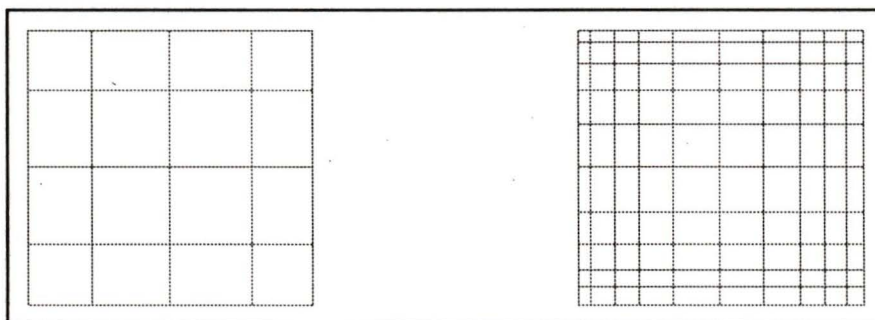


Figure 1.4: Example of Square Section Refinement. The left square has 4 grid points, and the right square has 10. Both have a geometric ratio of 1.3.

The coarser grid on the left has nearly uniform grid volumes because there are so few points over which the geometric ratio acts. In the finer grid, the volumes in the centre of the square are 4 times larger than the volumes in the corner. As can be seen more readily in the finer grid, the variables are solved over a much smaller physical space near the wall and thus are solved more accurately where their gradients are greatest.

1.6.2.5 Cost of Grid Refinement

The expense of grid refinement occurs in both problem size and computational time to generate the solution. A linearized solver, which uses explicit coupling, has a limited ability to distribute the information from the latest and best numerical solution to the other computational nodes in the domain. This is

governed more by the number of nodes to be solved at than by the physical spacing between nodes. Therefore more iterations are required to solve the same problem with a finer grid because the solver information travels more slowly through the physical domain. Secondly, more computational points occupy more memory in the computer performing the calculations. The greater the memory use, the greater the time required to access the memory. There are now two factors which dramatically increase the time required to solve the problem. In addition, computer memory is a finite resource and can be exceeded if care is not taken in the selection of the domain. If a large amount of memory is used due to grid refinement, then the physical area under consideration may have to be reduced so the total number of grid points does not exceed the maximum available to the computer.

1.6.3 Step Two - Differencing Scheme

A second important component of CFD that accompanies the grid refinement is the differencing scheme. The differencing scheme controls the order of accuracy of the numerical discretization as well as the "robustness" of the numerical solution. The simplest differencing schemes only share information between neighbouring grid points in the numerical solution. The more complicated and also more accurate schemes utilise points farther away from the current point of interest. A more accurate differencing scheme can produce better results with a coarser grid than the less accurate schemes with a much

finer grid. The penalty to be paid is that higher order and more accurate differencing schemes require more computation time. For this reason it may be better to spend computation time in differencing schemes instead of in finer grids. Whether the expense of higher order differencing schemes is more efficient than the grid refinement depends on the nature of the problem and the fluid behaviour that is involved.

1.6.4 Porous Sections

The porous wall effects were incorporated into CFX by attaching a thin porous region next to the wall or walls of the duct. As the heat transfer into the duct is also significant, a heat source can be provided within the porous section. The flow transpiration velocity, which is either injection or suction, was specified at the outside edge of the porous region. A schematic drawing of the problem is shown below:

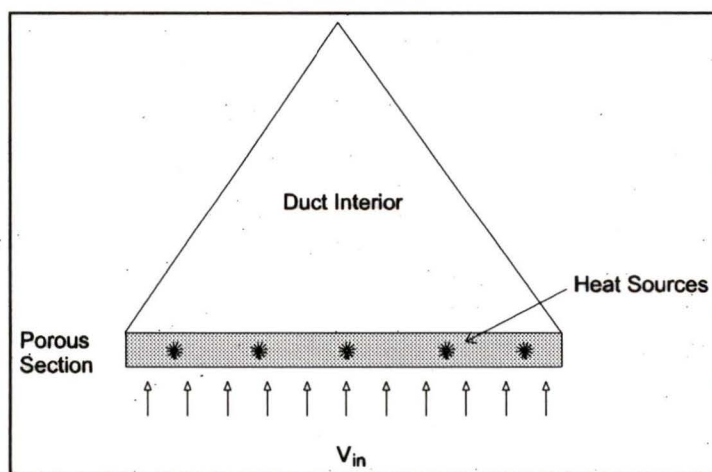


Figure 1.5: Cross-Section of Porous Section model

Alternatively, a pressure distribution was specified along the outer boundary of the porous layer and the flow through the porous layer is then computed based on this alternative boundary condition. Finally, a third boundary condition, which is diffusive and thus depends on local concentration conditions was implemented. The form of the boundary conditions was determined by results from the MEA model project concurrent to this project. The MEA model lead to reasonably independent boundary conditions that can be imposed on the channels. The problem itself is elliptic and hence boundary condition information passes both ways from the channel to the MEA, but for a given range of operation this variation proved to be sufficiently small to be negligible.

1.6.5 Multi Component Flow

The multi component flow aspect is important to this project and must be modelled for physically representative solutions. The multi component flow modelling is already included in the CFX code and is considered to be a strong point of the code. The amount of work outside of the code was unfortunately not minimal and while activation of the equations within the code was simple, appropriate boundary conditions could not be simply specified. The nature of the boundary conditions was determined from the MEA model, but considerable additional programming was required to create the appropriate boundary condition.

1.6.6 Integration with the MEA model

The final step in this project will be the integration of the flow channel modelling code with the full MEA model. There are several MEA models present in the literature [8], [12], [13], but they lack the flow channel detail of the present model. The combined model will represent the entire fuel cell and would be the most ambitious modelling project yet attempted. Computation times will likely require days on the resources presently available at the University of Victoria, but they may provide valuable information on the influences between the channel and the membrane and electrode assembly.

1.7 Porous Materials

Some background information on porous materials will be discussed in this section.

1.7.1 Porous Properties

Most work on porous media consider the medium to be described by two average properties: porosity and permeability.

1.7.1.1 Porosity

Porosity is a measure of the ratio between free space and solid occupied space inside the porous material. It is frequently expressed as a percentage or as a fraction with respect to 1. Typical porosity values are between 10% and 50% with some rocks approaching 1% porosity.

1.7.1.2 Permeability

Permeability is a measure of the ability of a fluid to flow through the porous material. There are at least two ways to visualize permeability. Permeability can be thought of as the effective area available to the flow. Permeability can also be viewed as a measure of the tortuosity of the paths through the porous material. A highly permeable material has short straight paths while a nearly impermeable material has long, sinuous paths. In this respect a decrease in permeability becomes more of an increase in path length rather than a decrease in flow area. An increase in path length for a simple path can always be transformed into an equivalent decrease in area for a constant length. Thus the units for permeability are those of an area. Permeability is linked to porosity by the fact that there is an upper bound on how much permeability a given porosity will permit. On the other hand, there is no limit to how small the permeability

may be because there is no material independent physical limit that requires the individual pore spaces to be connected.

1.7.2 Isotropy

All materials considered in this thesis are considered to be locally isotropic. This is given for porosity since there can not be anisotropy in a volumetric property.

A volumetric property is a property which depends on conditions over a volume.

An anisotropic property must vary in direction under consideration, but a volumetric property is independent of direction considered and thus is isotropic.

For permeability the justification for isotropy is simply that the materials considered are of sufficiently low permeability that they are unlikely to exhibit any sort of isotropy on the scales of motion considered. The permeability would have to be within 1/1000 of the facial area of the discretized volumes used, while the permeability considered is ten orders of magnitude smaller than the cell volume areas.

1.7.3 D'Arcy Flow

The most common approach to flow in porous media is the empirical D'Arcy's Law. The law assumes that all viscous effects from the fluid can be described by the resistance of the permeable material and the dynamic viscosity of the fluid.

This is expressed as:

$$Q = -\frac{k}{\mu} \frac{\partial P}{\partial x} \quad (6)$$

where k is the permeability, Q is the volumetric flow rate based on the material cross-section, μ is the viscosity of the fluid and $\frac{\partial P}{\partial x}$ is the pressure gradient.

This law does not consider any interactions between fluid elements as described by the Navier-Stokes continuum equations. D'Arcy's Law is however the limiting case of the general equations describing fluid flow through a porous medium. These general equations are the porous resistance modified Navier Stokes equations.

1.7.4 Navier Stokes Equations in Porous Materials

The Navier Stokes equations are modified in the momentum equation to account for porous flow [11]. The modification is in the form of a resistive force. Within CFX the default options for the resistive force are either constant, proportional to local velocity, or proportional to local velocity squared.

Beginning with the porous volume

$$\mathbf{V}' = \gamma \mathbf{V} \quad (7)$$

where γ is the volumetric porosity, the isotropic aspect of porosity leads to a modified area :

$$\underline{\mathbf{A}}' = \underline{\mathbf{K}} \cdot \underline{\mathbf{A}} \quad (8)$$

where $\underline{\mathbf{K}}$ is a symmetric second order tensor referred to as the area porosity tensor. The general scalar advection diffusion equation becomes

$$\frac{\partial}{\partial t}(\gamma \rho \Phi) + \nabla \cdot (\rho \underline{\mathbf{K}} \cdot \underline{\mathbf{U}} \Phi) - \nabla \cdot (\Gamma \underline{\mathbf{K}} \cdot \nabla \Phi) = \gamma S \quad (9)$$

where Φ is the scalar and Γ is its diffusivity. The porous flow modified Navier - Stokes equations are:

The modified continuity equation is

$$\nabla \cdot \underline{\mathbf{U}} = 0 \quad (10)$$

The modified conservation of momentum is

$$\nabla \cdot (\rho (\underline{\mathbf{K}} \cdot \underline{\mathbf{U}}) \otimes \underline{\mathbf{U}}) - \nabla \cdot (\mu \underline{\mathbf{K}} (\nabla \underline{\mathbf{U}} \times (\nabla \underline{\mathbf{U}})^T)) = -\gamma \underline{\mathbf{R}} \cdot \underline{\mathbf{U}} - \gamma \nabla p \quad (11)$$

In the limit of a large resistance, the anisotropic D'Arcy equation results in the form

$$\underline{\mathbf{U}} = -\underline{\mathbf{R}}^T \nabla p \quad (12)$$

where $\underline{\mathbf{U}}$ is the true fluid velocity and $\underline{\mathbf{Q}} = \underline{\mathbf{K}} \cdot \underline{\mathbf{U}}$

1.8 Physical Properties Considered

There is a vast range of physical parameters that could be considered in this thesis. To reduce this problem to a reasonable level, a set of parameters that are typical to fuel cell operation was selected.

Property	Value Considered
Porosity	0.4 ND
Permeability	4.73E-19 m ²
Inlet Reynolds Number	10-1000
Wall Reynolds Number	0.01 - 10
Hydraulic Diameter	0.001 m
Inlet Temperature	350 K
Inlet Oxygen Concentration	0.2 ND
Density	1.008 kg/m ³
Viscosity	2.072E-5 Pa/s

Table 1.1: Physical Properties and their Values

While the parameters may vary, the non-dimensionalization of most of the results allows for ready use of most results in the design of fuel cells. The only property which may require revision is the permeability. The value used of 4.73E-19 m² [8] is very small. Other materials with a value in this range are igneous rocks which are almost impermeable. It is conceivable that the value used for carbon fibre paper is smaller than the true value and may have been used as an adjustment parameter in previously reported work in order to obtain reasonable results with those models. There is no indication within the literature

that this occurred, but pure it is expected that a larger permeability value must be present in carbon fibre paper. The recommendations for further work include an accurate determination of the true permeability of the carbon fibre paper. This experiment will be a difficult undertaking, but accurate properties are crucial both to this model and to the combined MEA model.

Chapter 2 - Validation Work

2.1 Impermeable Wall Validation Work

Before any attempt to model the complex flow inside a fuel cell channel, efforts were directed towards validating the flow solutions from the CFX code against complex geometries. This work allowed the author to become familiar with the intricacies of a commercial CFD code while still producing results of some benefit to the overall understanding of the problem.

2.1.1 *Triangular Duct*

Most of the work was done on a triangular duct. The domain considered is illustrated below

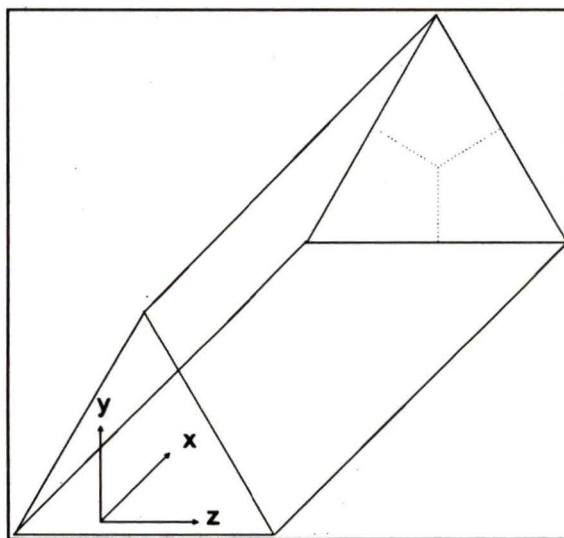


Figure 2.1: Domain considered for the triangular duct.

The goal of the work was to obtain some limits for grid refinement accuracy for non-porous flow and then use these results to confirm or direct later work that includes porous effects. The triangular grid was investigated mostly for fully developed effects because the three dimensional nature of the duct makes the computation of entrance effects very costly in terms of CPU time. A fully developed problem becomes 2-D and allows for extreme refinement without the excessive computational cost of a 3-D entrance problem.

2.1.2 Grid for Triangular Results

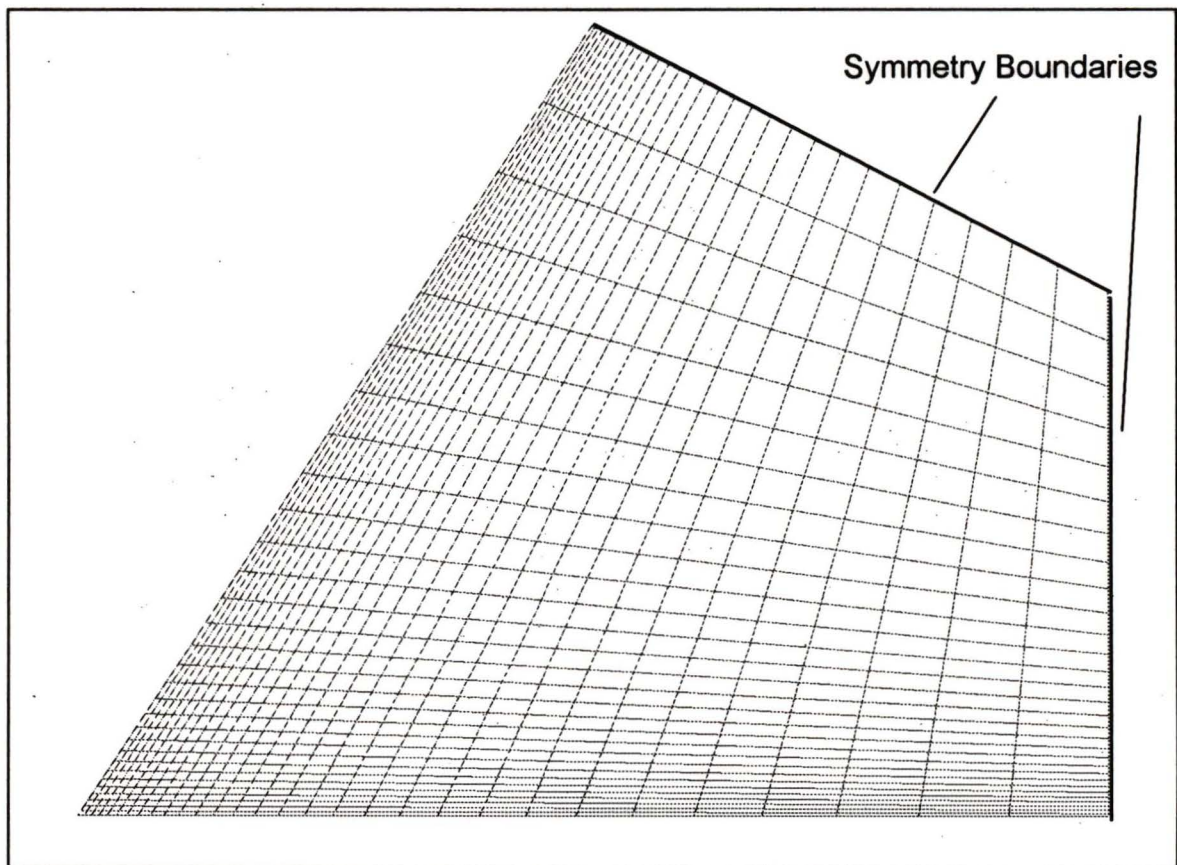


Figure 2.2: Grid for Triangular Duct. Note symmetry boundaries on the short sides of the quadrilateral

The grid used is a quadrilateral shape that exploits the three part symmetry in an equilateral triangle.

2.2 Results

2.2.1 Grid Refinement and Shear Force

Many numerical experiments were run for the triangular duct, but only a selection will be presented. The first results focused on grid refinement.

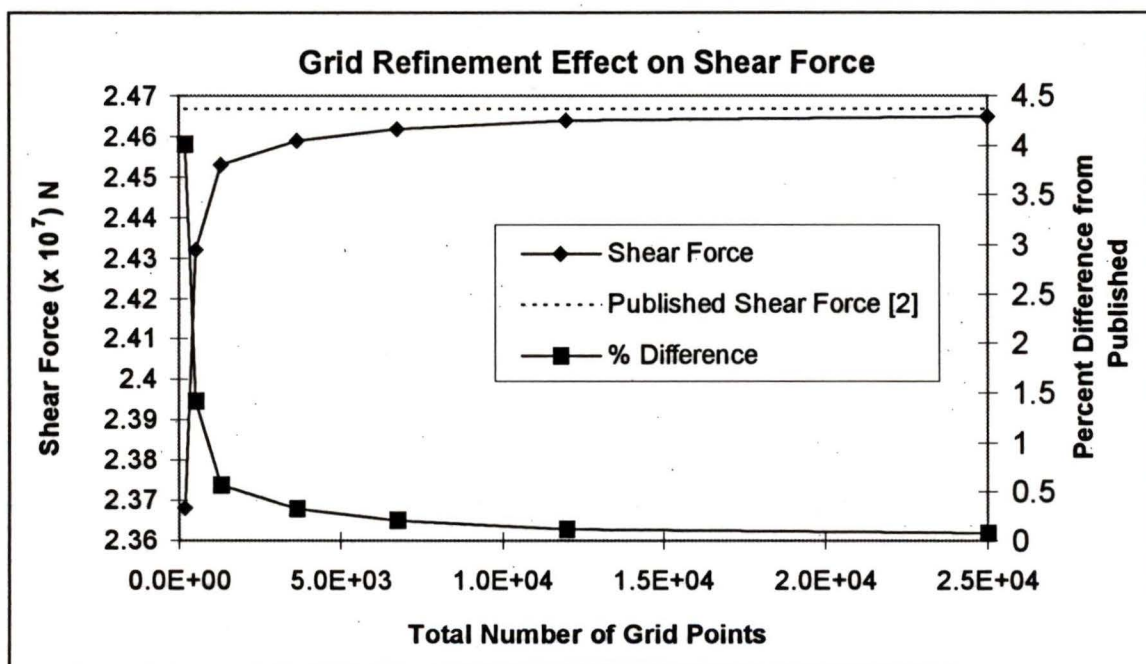


Figure 2.3: Grid Refinement Effects on Shear Force at the Solid Walls for an Impermeable Triangular Duct. The published data is from Kakac et al [2]

As can be seen from the figure above, there is an exponential effect on the total shear force exerted on one wall of the duct as a function of grid refinement.

There is little improvement beyond the 5000 total point grid, at least in consideration of the number of grid points required.

2.2.2 Heat Transfer

The next step in the model was to create a heat transfer model that would investigate the effect of grid refinement on thermal aspects of the problem. The same cross sectional grid was used, however, it was necessary to extend the problem to three dimensions so that the thermal effects could be considered. The heat transfer boundary conditions permitted within CFX do not allow for a quasi two dimensional simulation in order to generate fully developed results. Therefore a fully developed velocity profile was used, which allowed the thermal boundary layer to develop untouched by the momentum boundary layers. This setup permitted rapid convergence for a three dimensional problem because the non linear momentum equations were still reduced to two dimensional, while the three dimensional thermal problem is a scalar for incompressible constant property flow and hence is easily solved.

2.2.2.1 Nusselt Number

The Nusselt number is a non-dimensional number used to represent the heat transfer ability of a particular duct. Heat transfer problems frequently have several different boundary conditions that influence the non-dimensionalized results. The most common boundary conditions are constant wall temperature

and constant heat flux. For a fuel cell with constant heat generation along the entire duct the constant heat flux boundary condition would be most relevant. For a true fuel cell this corresponds to a single wall with a constant heat flux, for the symmetrical problem considered, only uniform heat flux around the circumference of the duct can be considered. The other configuration with one adiabatic wall is not physically meaningful. For a constant heat flux the Nusselt number is based on the average duct temperature, and the average wall temperature of the walls under heat flux. In a non-dimensional form this leads to:

$$Nu = \frac{1}{\theta_w - \theta_b} \quad (13)$$

$$\theta_b = \frac{1}{u} \int_0^1 \int_0^1 u \theta \, dy \, dz \quad (14)$$

$$\theta = \frac{T}{T_o} \quad (15)$$

where T_o is the reference or in this case, the inlet temperature.

2.2.2.2 Differencing Schemes

Two differencing schemes were compared in the validation work to determine if modifications in this aspect of the computational procedure could lead to benefits in the computational time required for calculations. The background to the schemes will be discussed first with reference to the following computational stencil. The stencil is drawn with a uniform grid, however, there are straightforward extensions to uniform grids.

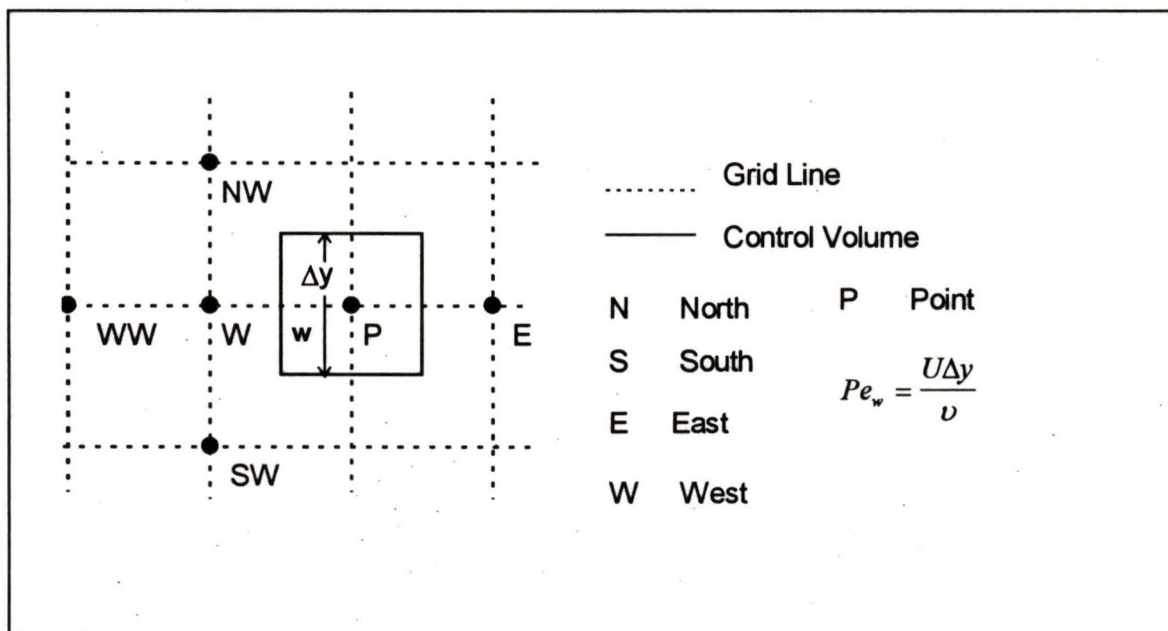


Figure 2.4: Computational Stencil for Evaluating Fluxes under Various Differencing Schemes.

2.2.2.3 Hybrid Differencing Scheme

Two differencing schemes were considered: Hybrid and CCCT. The Hybrid scheme is discussed first. It is a popular scheme in computational fluid dynamics because it is robust and frequently quite accurate. The Hybrid

scheme was developed by Spalding [14] in 1972 as an attempt at combining the robust but only first order accurate upwind differencing scheme with the more unstable but second order accurate central differencing scheme. A good discussion of the scheme also appears in Patankar's book [15]. The upwind scheme utilizes, as an approximation of a face value, the point on the upstream side of the face under consideration. The central differencing scheme uses the average value of the two points closest to the face under consideration. The two points are weighted in the contribution by their proximity to the face under consideration. Finally, the Hybrid differencing scheme approximates terms at a grid face by using a central difference when the absolute value of the local Peclet (Pe) number is small, and a simple upwind value when the absolute value of the local Peclet number is large.

Differencing Scheme	Value of U_w
Central Difference	$0.5(U_w + U_p)$
Upwind $Pe > 0$	U_w
Upwind $Pe < 0$	U_p
Hybrid $Pe > 2$	U_w
Hybrid $Pe < -2$	U_p
Hybrid, $ Pe \leq 2$	$0.5(U_w + U_p)$

Table 2.1 Approximation of Face Value for Various Differencing Schemes.
A uniform grid is assumed for central differencing.

The critical Peclet number is 2. The computational stencil in Figure 2.4 can be used to illustrate the Hybrid Scheme. If the value of U velocity at the face w is desired then the Peclet number at that face, $Pe_w = \frac{U\Delta y}{\nu}$ is a measure of the convective versus diffusive fluxes through the face w. If the absolute value of this number is greater than 2 then the upwind scheme is used because convection is stronger than diffusion, while if the absolute value of the Peclet number is less than 2 then the central difference is used. Raithby [16] demonstrated that the Hybrid scheme has poor accuracy when the flow is not perpendicular to the grid used, but in the flows of interest, the largest component of the flow is perpendicular to the grid.

2.2.2.4 QUICK Scheme

The second scheme considered was the CCCT scheme. The CCCT scheme is a modified QUICK scheme, so the background to the QUICK scheme will be discussed first. The QUICK scheme, which is third order accurate for convection terms and only second order accurate for diffusion, was first proposed by Leonard [17]. It features a quadratic interpolation polynomial fitted to two upstream points (based on local flow conditions) and one downstream point for the face considered. Referring back to the computational stencil in Figure 2.4, if the flow is arriving at face w from the west direction, then the value of U at w is based on a quadratic polynomial fitting to points P, W, and WW. If the flow were

arriving instead from the north-west direction then the value of U would be based on the points P , W and NW with appropriate quadratic weighting. The QUICK scheme has been found to be very stable and reduce the numerical diffusion caused by the non-orthogonality of the flow to the grid [16]. While the QUICK scheme is generally well behaved, it is not bounded and can give rise to unphysical overshoots, which lead to numerical instability. To correct for this unphysical behaviour many modifications which bound the QUICK scheme to physically meaningful values have been proposed.

2.2.2.5 The CCCT Scheme

The CCCT is one of the more recent modifications to the QUICK scheme. It employs a weighting parameter based on the curvature of the local flow, to ensure that only physically meaningful bounded values are generated. It was developed by Alderton and Wilkes [18] and the details of the weighting parameter calculation are found in [11].

2.2.3 Differencing Results

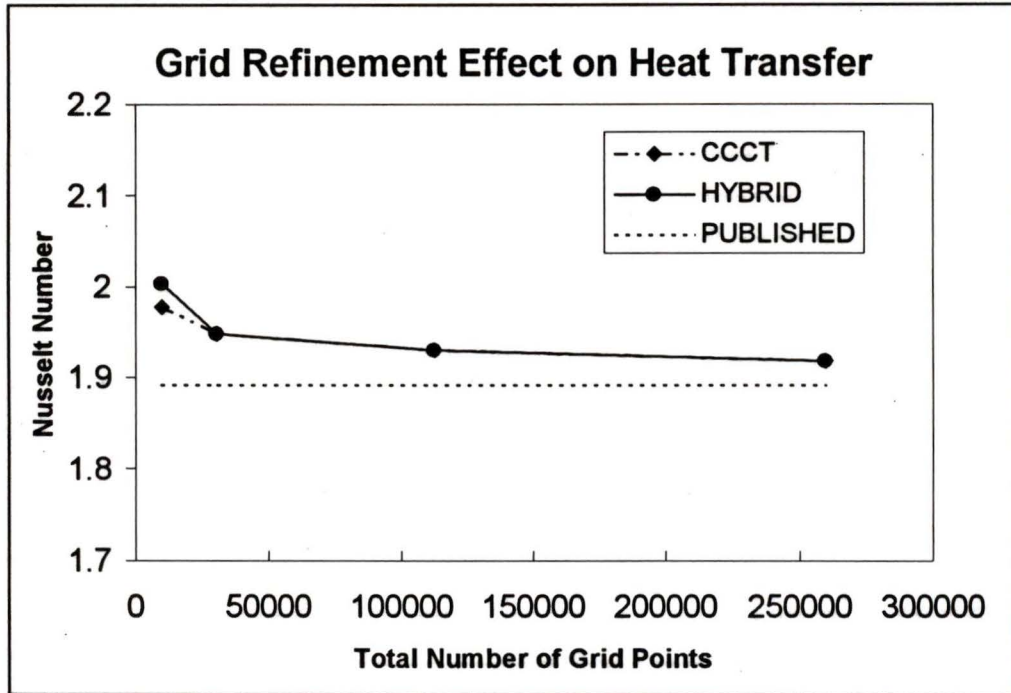


Figure 2.5: Grid Refinement and Differencing Scheme Effects on Heat Transfer. The Nusselt number is based on a constant heat flux.

The differencing scheme was found to be important only at lower levels of grid refinement. The higher order CCCT scheme, which is the most accurate scheme available within CFX, provided a slightly more accurate solution to the Nusselt number at the grid point level of 100. The solution, however, is still less accurate than a hybrid scheme at a greater grid refinement and at 30,000 grid points, the solutions are identical. The indifference of the solution to various differencing schemes is explained by the simple nature of the unidirectional laminar flow. There is no flow in either the Y or Z directions and hence there is

no curvature to the flow. The higher order differencing schemes are only of benefit when there is considerable curvature to the flow, which can be better approximated with a higher order differencing scheme.

2.2.4 Grid Refinement Results

The grid refinement shows that there is little improvement in heat transfer predictions for a large increase in the grid density past the grid point level of 30,000 total points. The results are within 3% of the published solution at this level and that is sufficiently accurate considering there are other approximations within the present model.

2.3 Permeable Wall Validation

The next step in validating the CFX results was to compare to a simple porous wall problem. The simplest problem available is the problem of infinite porous plates with identical suction or injection.

2.3.1 The Berman Solution

A.S. Berman [4] was the first to theoretically investigate two dimensional flow between porous parallel plates. The geometry of this problem is shown below.

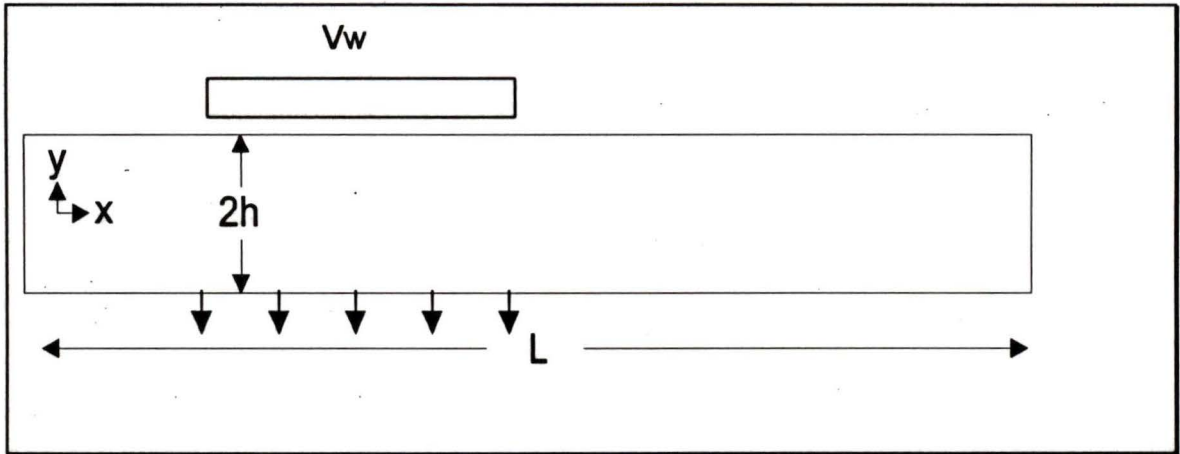


Figure 2.6: Illustration of the parallel plates considered by Berman

Berman treated the problem with a stream function approach and used a perturbation technique to generate an analytical solution to the problem. The perturbation approach yields answers that are more valid for small perturbations. This solution is relevant to the problem under study in this thesis because the wall velocities are very small with respect to an impermeable wall problem. The form of the Berman solution is as follows:

$$u(x, \lambda) = \left[\bar{u}(0) - \frac{v_w x}{h} \right] \left[\frac{3}{2}(1 - \lambda^2) \right] \left[1 - \frac{R}{420}(2 - 7\lambda^2 - 7\lambda^4) \right] \quad (16)$$

$$\frac{v(\lambda)}{v_w} = \frac{\lambda}{2}(3 - \lambda^2) - \frac{R}{280} \lambda(2 - 3\lambda^2 + \lambda^6) \quad (17)$$

where

$$\lambda = \frac{y}{h}, \quad R = \frac{v_w h}{\nu} \quad \text{and} \quad \bar{u} = \frac{1}{h} \int_0^h u \partial h$$

2.3.2 Comparison with the Berman Solution

A numerical model corresponding to Berman's configuration was set up and the two-dimensional results were compared with the analytical results of Berman.

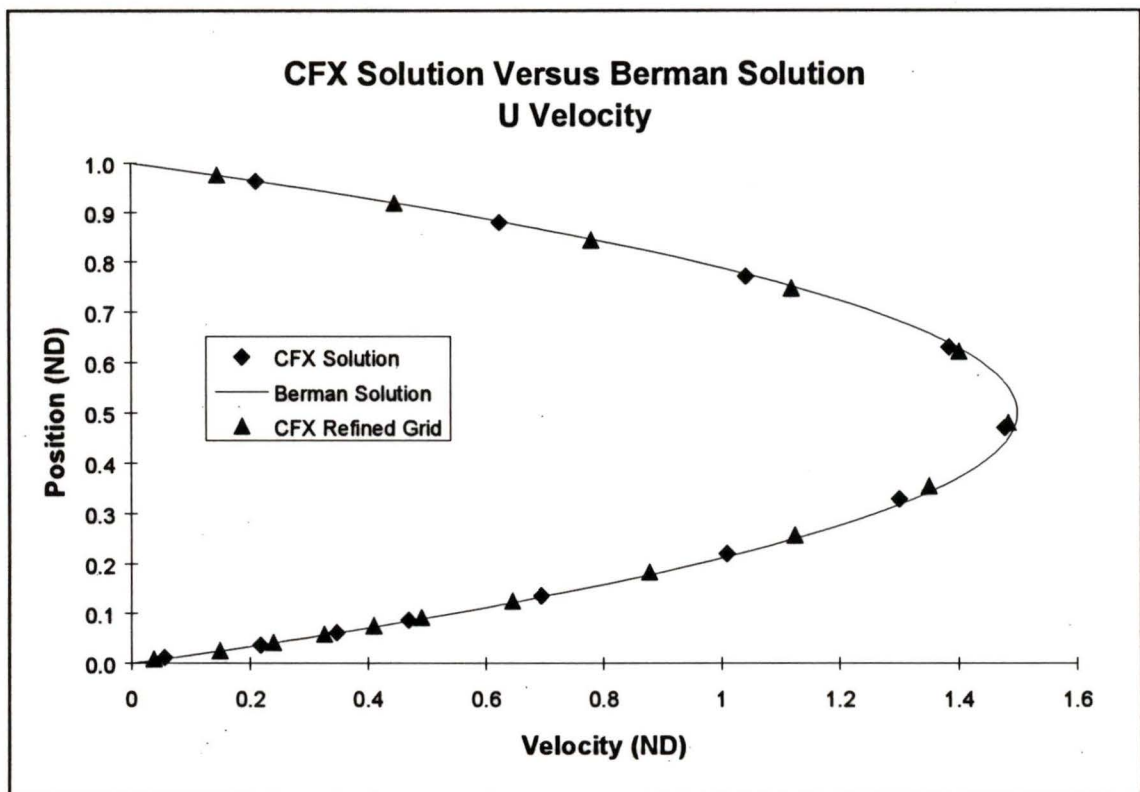


Figure 2.7: U Velocity Comparison between permeable wall model and the Berman solution

The U Velocity results from the present model are in excellent agreement with the analytical results, indicating that the present model is accurate for the flow

solution. Furthermore the coarse grid of 11 cross stream points results in a solution that is nearly identical to the more refined solution of 16 points. The resolution required for the flow in the porous duct with low wall velocities is therefore similar to that for non-porous ducts.

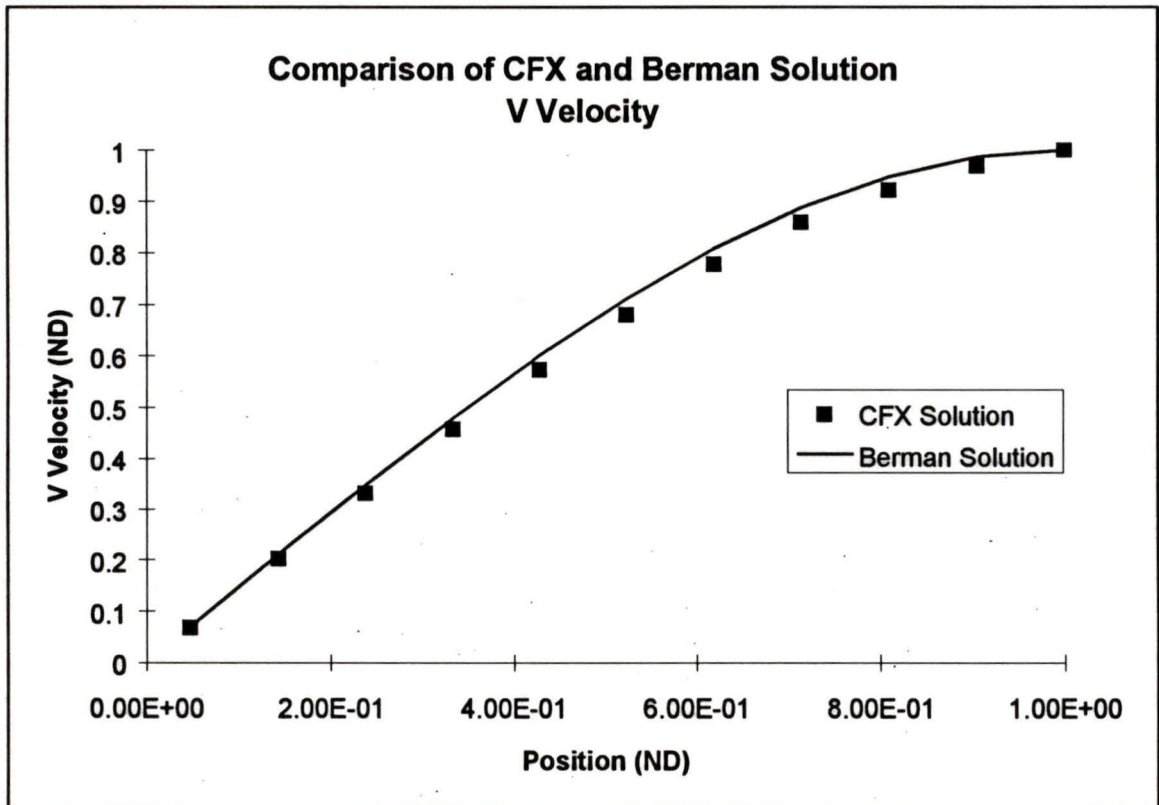


Figure 2.8: V Velocity Comparison between permeable wall model and the Berman solution

The graph of V Velocity distribution across the duct shows a similar comparison to the U velocity. A grid refinement comparison was not used because it was felt that sufficient effort had been expended in assessing grid sensitivity. The V velocity results show slightly more deviation than the u velocity results, however,

the v velocity is two orders of magnitude less than the u velocity ($v < 1\% u$), hence the relative differences may be larger, but the global differences are still minimal. The results are better immediately next to the wall and near the centre of the duct. This indicates that further grid refinement in the middle of the duct from 0.3 to 0.8 ND would probably generate a better result. The improvement would not be sufficient to warrant the additional computational expense. The conclusions that can be drawn from these results is that the coarser grid can be used to generate sufficiently accurate solutions, and the CFX model compares very well to the analytical Berman solution, for the small wall velocities considered here. It is expected that some discrepancies will occur at higher wall velocities for which the assumptions in Berman's solution are no longer valid. The numerical model, on the other hand, is not limited in this manner.

Chapter 3 Adding a Porous Section

3.1 Need for a Porous Section

A porous section is necessary to model heat transfer into the duct. It is also needed to model the complex hydrodynamic effects at the interface between a porous medium and a duct. The simple permeable wall model does not have the complex heat transfer boundary conditions that may be required. It is completely incapable of modeling the interface conditions with the porous medium.

3.2 Definition of a Porous Interface

The conditions at the porous wall interface are still the subject of some active research. The conditions at this interface are complex and even defining the boundary itself is a non trivial matter. The most common method of defining the boundary is the point at which there is no longer any microscopic porous material in directions parallel to the macroscopic porous surface. This definition seems straightforward, and in a theoretical sense it is; implementation into a practical situation is somewhat more difficult. A diagram illustrating this aspect of the boundary definition is shown below.

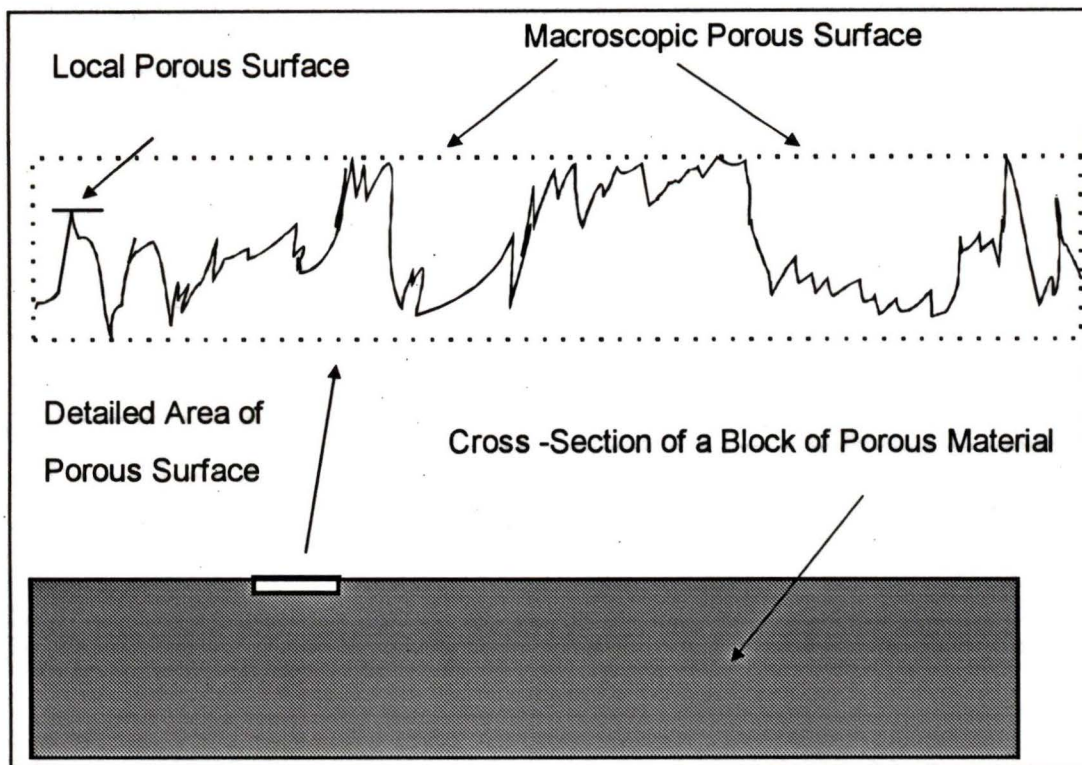


Figure 3.1: Detailed View of the Surface of a Porous Material

From the diagram it can be seen that the local porous surface is a variable quantity that changes with position along the porous surface. Hence the local definition of the porous surface is not used to describe the overall porous material boundary, rather the macroscopic porous surface is used. As a result of using the macroscopic surface, an attempt must be made to describe globally how the macroscopic peak porous surface relates to the distribution of local porous surfaces. Some materials may have a very uniform local porous surface distribution and hence the macroscopic surface is very close to the local surface at any particular location. At the other extreme the distribution of local porous surfaces may be so arbitrary that the macroscopic porous surface may be far

removed from most of the local surfaces, while still representing the average surface location. Obviously different solutions near this porous interface will result when the true local porous surfaces differ, even if the macroscopic porous surfaces are identical and the average porous properties of the material are identical. Hence another parameter is required to describe the porous material which is not a property of the material in general but relates more to the history and variability of the material at a free surface of the material. After considering the factors determining the fluid dynamics at a porous interface, several ad hoc definitions of a parameter, commonly denoted by α in a non-dimensional form [19,20], have been proposed.

3.3 Integrating α into the fluid dynamics

The boundary between channel and porous section is the macroscopic porous surface. The porous material is isotropic and thus permits flow both parallel to the macroscopic surface and perpendicular to it. Since the channel boundary is also the porous surface, the non zero parallel velocity is termed a slip velocity with respect to the boundary of the channel. This aspect of the velocity profile is shown below in Figure 3.2.

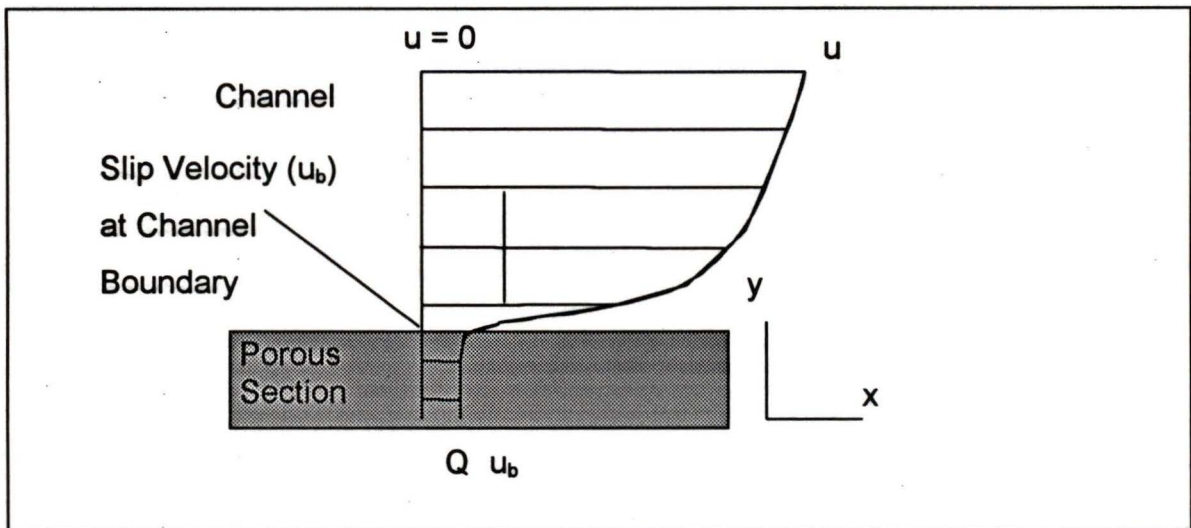


Figure 3.2: Illustration of Velocity Distribution Inside a Porous Section and into the Surrounding Channel.

The slip velocity can be an important factor governing the velocity distribution within the duct. More importantly, even small slip velocities have large effects on concentration distributions [21]. By an inspection of the slip velocity it can be seen that it will depend firstly on the permeability of the porous material, which governs the pressure drop for a given velocity; permeability determines the magnitude of Q . Secondly the slip velocity depends on the α parameter, which determines the distance required to develop the average permeability; α determines the difference in velocity from Q to u_b for that particular sample of porous material.

3.3.1 The Beavers and Joseph Solution

The first attempt at integrating α into a fluid dynamics solution was by Beavers and Joseph [19]. They derived an expression for the slip velocity by relating it to the shear stress at the porous wall and the average parallel flow rate along a porous material. Starting from D'Arcy's Law

$$Q = -\frac{k}{\mu} \frac{\partial P}{\partial x} \quad (18)$$

and using the ad hoc boundary condition

$$\frac{\partial u}{\partial y} \Big|_{y=0^+} = \beta(u_b - Q) \quad (19)$$

defining a non-dimensional slip parameter gives

$$\alpha = \beta \cdot \sqrt{k} \quad (20)$$

the Poiseuille flow in the channel is governed by

$$\frac{\partial^2 u}{\partial y^2} = \frac{1}{\mu} \frac{\partial P}{\partial x} \quad (21)$$

with the complete set of boundary conditions:

$$u = 0 \text{ at } y = h \quad (22)$$

$$\frac{\partial u}{\partial y} = \frac{\alpha}{\sqrt{k}}(u_b - Q) \text{ at } y = 0 \quad (23)$$

The solution of the above gives the result

$$u = u_b \left(1 + \frac{\alpha}{\sqrt{k}} y \right) + \frac{1}{2\mu} (y^2 + 2\alpha y \sqrt{k}) \frac{\partial P}{\partial x} \quad (24)$$

$$u_b = -\frac{k}{2\mu} \left(\frac{\sigma^2 + 2\alpha\sigma}{1 + \alpha\sigma} \right) \frac{\partial P}{\partial x} \quad (25)$$

where $\sigma = \frac{h}{\sqrt{k}}$.

The fractional increase in mass flow rate through the channel for a given pressure gradient over what the rate would be without the porous section i.e. the increase due to the slip velocity at the porous interface is given by

$$\Phi = \frac{3(\sigma^2 + 2\alpha\sigma)}{\sigma(1 + \alpha\sigma)} \quad (26)$$

In most applications h will be much larger than \sqrt{k} ($\sigma \gg 1$) so the equations should be valid. When the height of the channel approaches the height of the interstitial gaps in the porous material σ will approach $\sqrt{2}$ and Φ will have a value of 3. The additional properties of such a σ are that the slip velocity is equal to the D'Arcy velocity within the permeable material and there is no

velocity gradient at the permeable wall. Hence the assumption of rectilinear Poiseuille flow will no longer be valid. The limiting condition for the break down of the Poiseuille flow assumption is when the channel height approaches the size of the pore space within the porous medium. The conditions considered for this thesis do not involve such relative sizes of h and k so the assumptions of Beavers and Joseph apply to the problems considered.

3.3.2 The Saffman Solution

An alternative boundary condition was later proposed by Saffman [20]. Saffman based his recommendation on an investigation into the approximations made by assuming a slip velocity boundary condition. He found the error introduced by his approximation was of the same order of magnitude as the Beavers and Joseph approximation because their approximation only reduced in order of error when the boundary condition was specified at exactly the correct location. Thus there is no gain in using the extra D'Arcy velocity term in Beavers and Joseph. The Saffman boundary condition is

$$u_b = \frac{k^{1/2}}{\alpha} \frac{\partial u}{\partial y} + \text{Truncation Error } O(k^{1/2})$$

(27)

in contrast to

$$u_b = \frac{k^{1/2}}{\alpha} \frac{\partial u}{\partial y} + Q + \text{Truncation Error } O(k)$$

(28)

3.3.3 The Exact 2-D solution

There was a considerable lull in the activity into porous media boundary conditions until a resurgence occurred in 1990. Vafai and Kim [22] published an exact solution to the flow solution near a porous medium for a 2-D problem. Their work assumed that the porous medium was infinite in the y direction and included the effect of an inertia parameter.

The inertia parameter depends on the pore structure of the porous medium and the pore Reynolds number. This inertia parameter more accurately models the losses which are frequently merely lumped into the D'Arcy equation and thus over simplified. However, the simplification is appropriate when the pore Reynolds number is small enough. The general rule is that if the pore Reynolds number $Re_p = \frac{Qk^{1/2}}{\nu}$ is less than 0.1, then the inertial effects are negligible. For the materials and flow rates under consideration $Re_p = 10^{-10}$ and hence is much less than 0.1.

The Vafai analysis resulted in a solution for the velocity distribution of

$$u = -\frac{A+B}{2}y^2 + \left(u_i + \frac{A+B}{2}\right)y \quad (29)$$

where y is the distance from the solid wall towards the porous section, u_i is the interface or slip velocity, and

$$A = \text{Re}_H \Lambda_H \quad (\text{Inertia Parameter}) \quad (30)$$

$$B = \frac{1}{\text{Da}_H} \quad (\text{Permeability Parameter}) \quad (31)$$

$$\text{Da}_H = \frac{k}{H^2} \quad (32)$$

To obtain the interface velocity, the first derivative of velocity, i.e. shear, is assumed to be continuous across the interface and

$$-\frac{A+B}{2} + u_i = -(u_i - 1) \sqrt{\frac{2A}{3} \left(u_i + 2 + \frac{3B}{2A}\right)} \quad (33)$$

By taking the limit of equation 33 where the permeability approaches 0 and the inertia parameter is zero leads to

$$u_i = \frac{\sqrt{B}}{2} \quad (34)$$

or in a dimensional form $U_i = \sqrt{\frac{H^2}{k} \frac{k}{2\mu} \frac{dP}{dx}}$

Substituting in for the known parameter values for the problems under consideration leads to a slip velocity of $1E-6$ m/s. In comparison, the transverse velocities at the porous wall have a value of $1E-5$ m/s. Clearly if the transverse velocities are important, then the slip velocity must also be important. The slip velocity is most important as it approaches zero. This can be rationalized by inspecting the percentage change of the slip velocity. For the slip velocity to change from zero to any number is an infinite percentage change.

3.4 Porous Section Boundary Conditions

The porous section requires different boundary conditions than the permeable wall model.

3.4.1 Velocity Boundary Condition

The velocity boundary condition must be changed to reflect the reduced porous area inside the porous region. The velocity must be increased by a factor equal to the $2/3$ root of the volume porosity which is the area porosity.

If L_p, A_p, V_p are the length, area, and volume porosity then

$$A_p = L_p^2 \text{ and } V_p = L_p^3 \quad \Rightarrow \quad A_p = V_p^{2/3}$$

Therefore

$$v_p = \frac{v_o}{V_p^{1/3}} \quad (35)$$

where v_p is the porous velocity and v_o is the original boundary velocity.

3.4.2 Heat Transfer

The initial implementation of the duct into a CFD model involved using a solid wall, which permits the specification of heat flux boundary conditions. As we move to a porous wall model, the CFX software permits either a specified mass flow or a specified velocity boundary condition. In either case, the heat flux through the porous wall can no longer be specified. The only thermal boundary condition permissible is a specified temperature, which is of course unknown.

With a porous section, the heat flux can be specified over a single grid volume, which is a better approximation than attempting to calculate a temperature for the permeable wall.

3.5 The Porous Section Model

The complete coupled porous section model is illustrated in the following figure. It shows all the impermeable walls, the porous interface as well as the catalyst layer that now forms the boundary for mass transport external to the model.

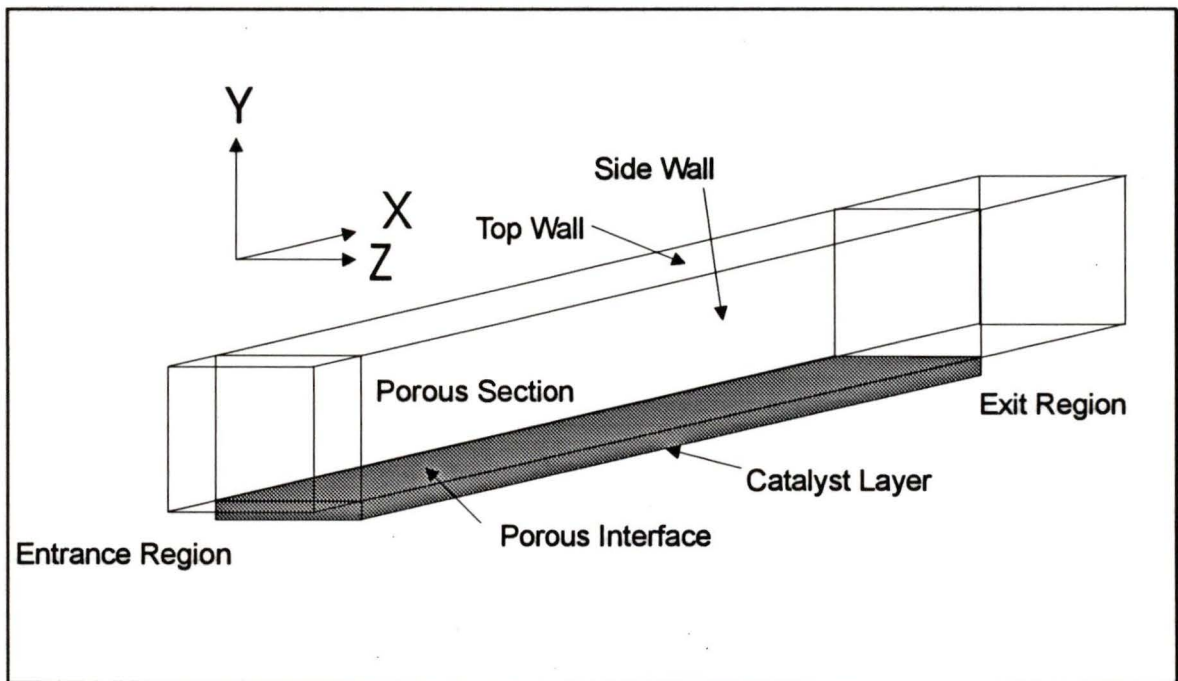


Figure 3.3: Porous Section Model

3.6 Porous Section Grid

The new coupled porous section required additional effort in the grid generation. It was found through trial and error experimentation and through in depth queries to the CFX support staff that the accuracy of the CFX method for calculating wall and inter block effects depends on the uniformity of the grid at the interface. Because the porous interface is crucial to the entire flow solution, it was therefore to have a uniform grid at the interface to the porous section. This was

accomplished by further dividing the duct into an interface region and a core region.

3.7 Slip Velocity Results

3.7.1 Implementation of the Vafai Slip velocity

The Vafai slip velocity was implemented using a uniform near interface grid and a geometric ratio of 0.7 away from the interface within the porous region. The results for identical grids with and without the specified slip velocity were plotted for comparison in the figure below.

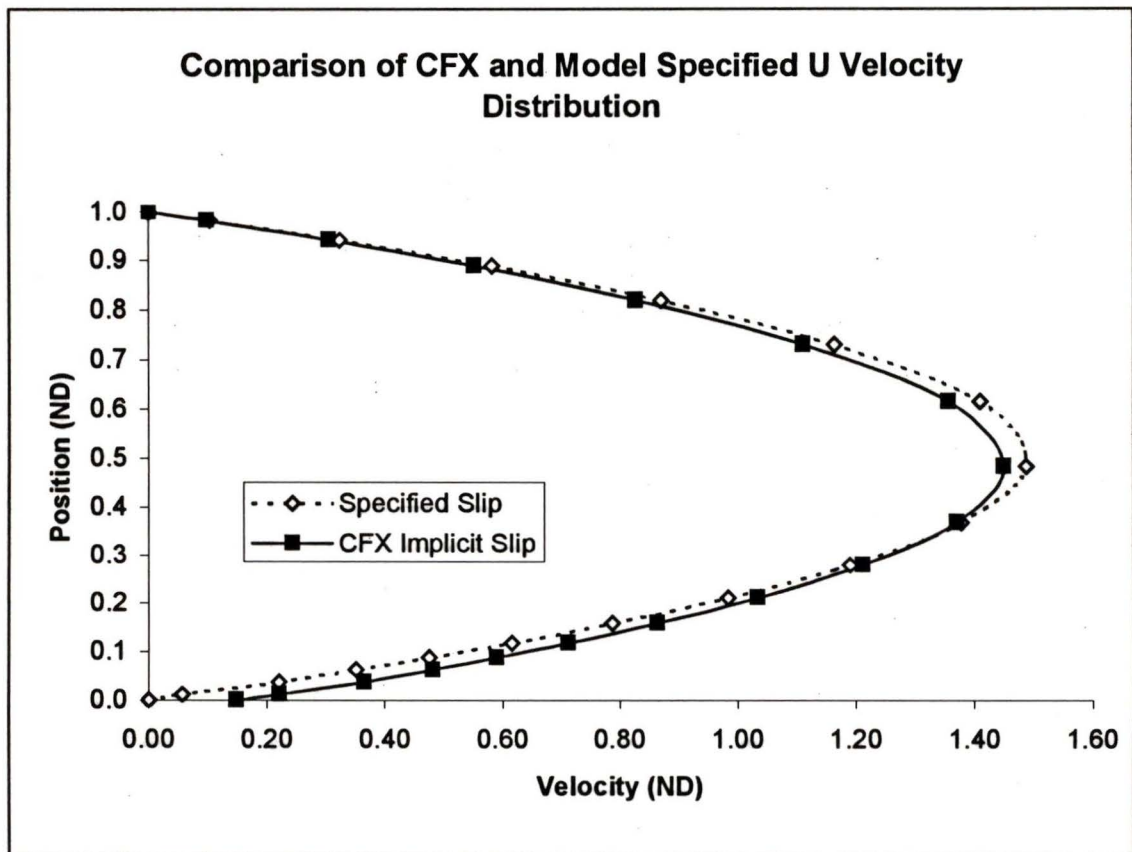


Figure 3.4: Slip Velocity Comparison between present model and CFX default

The comparison shows the slip velocity has a significant effect throughout the velocity distribution. At the porous interface (Position = 0), there is a difference between the Vafai and CFX slip velocity of 0.15. The relative difference is 15% of the average velocity and approximately 70% when compared to the local velocity at the first grid point used. The effect at the centreline is smaller, but the peak velocity is still decreased by 5%. The implications to shear stress, and by analogy to mass transfer, are very significant since these quantities are determined by the gradients at the interface. These results indicate the importance of modifying the CFX code to include the proper slip velocity in the model.

3.7.2 Grid Resolution

Despite the efforts to improve the solution at the porous section interface, adequate results for an apparently reasonable grid were not forthcoming. It was therefore necessary to investigate the effect of grid refinement in the vicinity of the porous region. This refinement was accomplished in a different manner than the refinement in the non-porous ducts. In this case the grid was composed of three discrete segments, a main channel with a large geometric ratio between grid points, a uniformly gridded section near to the interface, and a non-uniform grid with a moderate geometric ratio inside the porous section. The grid was most refined near to the porous interface. The grid refinement was

accomplished by decreasing the physical size of the uniformly gridded near porous section and then adjusting the geometric ratios in the main channel and the porous section in order to have a smooth transition on both sides of the uniform section. Figures illustrating a very coarse and a very refined grid are shown below to illustrate this process.

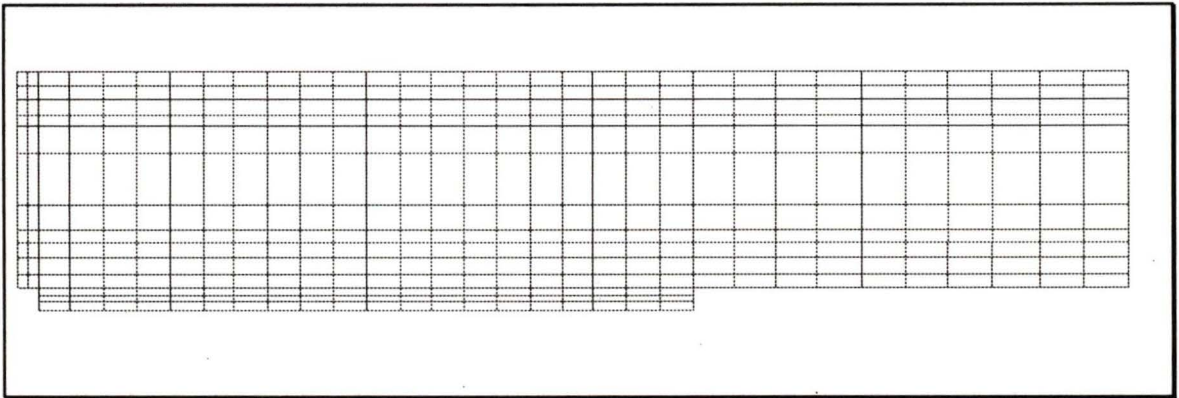


Figure 3.5: Coarse Grid in X and Y directions for Coupled Porous Section

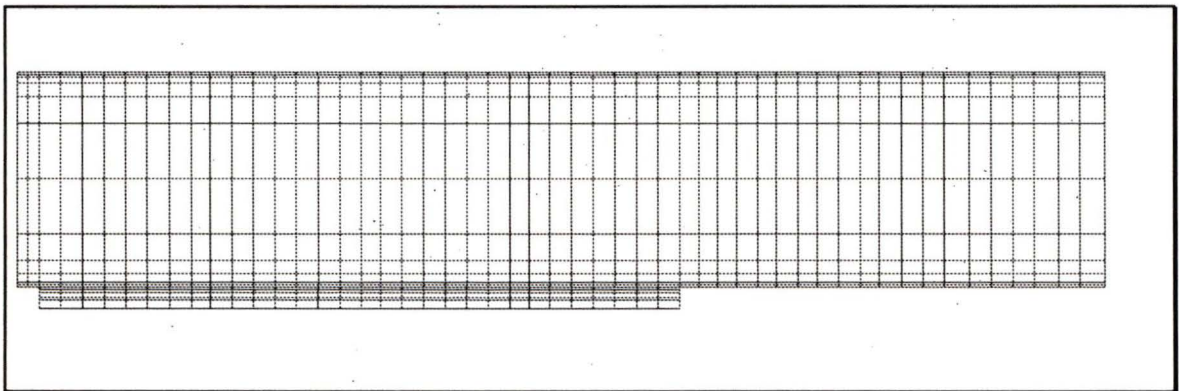


Figure 3.6: Fine Grid in X and Y directions for Coupled Porous Section

The percent difference between the velocity at a the first node into the near porous section for a case with a porous section and a solid wall were plotted

against the distance from the interface / solid wall to the first node. As can be seen clearly on the graph, this near-wall refinement has a significant effect on the solution. Once a distance of 5 μm (0.005 ND) is achieved, the results are within one percent of each other.

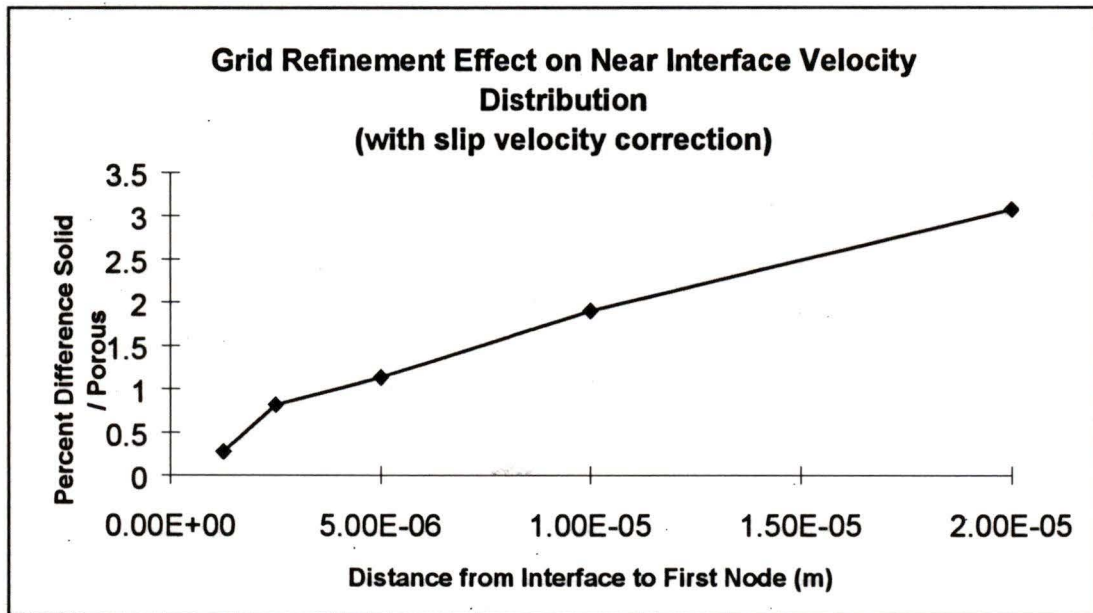


Figure 3.7: Effect of Grid Refinement on Near Interface Velocity

Once the grid has been refined to this degree, the geometric ratio between grid points inside the duct has reached a value of around 2.0 when values of 1.3 are recommended. Certainly in the immediate vicinity of any other walls in the domain this ratio is unacceptable. To match the refinement near the porous interface, the same small uniform grid used at the interface is also used at the wall opposite to the porous section. In this way, the shear stress and hence velocity distribution will be similarly resolved in the two critical areas.

3.8 Convergence within Porous Sections - Double Precision Variables

The convergence of a numerical solution can be expressed in terms of a residual. The residual is simply the difference between the terms on one side of the equation under consideration and the terms on the other side. In the case of the mass equation, one side is the divergence of the velocity, and the other is the expected result of zero. The inlet conditions for this model are expressed in units of kg/s, which are of the order of $1\text{E-}6$. A converged solution will have mass residuals, which are at least five orders of magnitude less than the inlet conditions: values of around $1\text{E-}11$. The numerical solution is driven by the $R^{-1} \nabla p$ effect within the porous section. Since R is very large and ∇p is also very large, problems with numerical accuracy can easily arise. For large suction or injection flows (e.g. $\text{Re}_w = 1$), single precision variables were found to produce a constant value in the mass residual of around $1\text{E-}6$ kg/s which is a worse solution than the inlet conditions could possibly physically provide. Therefore, some means to improve the convergence was needed. A double precision implementation was utilized to determine if the constant behaviour of the mass residual was due to numerical precision limits, or some greater effect. It was found that double precision enabled the solution to improve beyond the $10\text{E-}6$ barrier and lead to a stable well behaved convergence path. Final residuals were in the range of $1\text{E-}11$ to $1\text{E-}13$ depending on the injection/suction velocity.

3.8.1 Additional benefits of Double Precision Variables

An additional benefit of the double precision implementation as mentioned in the CFX manual was improved convergence rate. Table 3.1 shows the differences in solution times. For this case, a smaller Re_w value ($Re_w = 0.001$) was used in order for the single precision version of the model to have some measure of convergence to compare with the double precision version.

	Single Precision	Double Precision	Percent Difference
CPU Time per Iteration	6.76 s/it	8.52 s/it	-26 %
Iterations to $1e-10$	93 its	71 its	+23 %
Time to $1e-10$	628 s	605 s	3.7%

Table 3.1: Computational Time Comparison between Single Precision and Double Precision variables. The case considered was a 2D Single Component Case with Modified Slip Velocity and $Re_w = 0.001$

From the table, CPU time per iteration increased, but the rate at which the solution improved from iteration to iteration exceeded the penalty in CPU time per iteration. The increase in CPU time per iteration was caused by the increased memory access times, while the iteration efficiency was increased by the accurate resolution of the small but important V and W velocities.

Chapter 4 Single Component Results

After that the model incorporated the slip velocity effect, it was used to generate some single component results. These results were compared with the permeable wall numerical and experimental results of Cheng, noting however, that the Cheng numerical model does not incorporate a slip velocity.

Furthermore, the Cheng model utilized a space marching scheme, which ignores the elliptic nature of the Navier Stokes equations. The space marching solution procedure assumes that variations only travel in one direction. The numerical methods required for a solution are thereby much simpler because the spatial coupling of the governing differential equations has been reduced. This assumption is, however, quite valid for unidirectional internal flows; some of the differences between the present model and the Cheng model can be associated with the different forms of the Navier Stokes equations (parabolized versus full). The results are compared only with the Cheng data because that is the only data available in public literature that incorporates most of the effects that are included in the present model. Experimental data is very scarce in this area of fluid dynamics.

4.1 Two Dimensional Results

The two dimensional results will be presented first.

4.1.1 Domain Considered

Due to the finite memory available on the computer used for this model, a restricted domain was used. The domain consisted of a duct length of 70 times the hydraulic diameter of the duct. This is illustrated below.

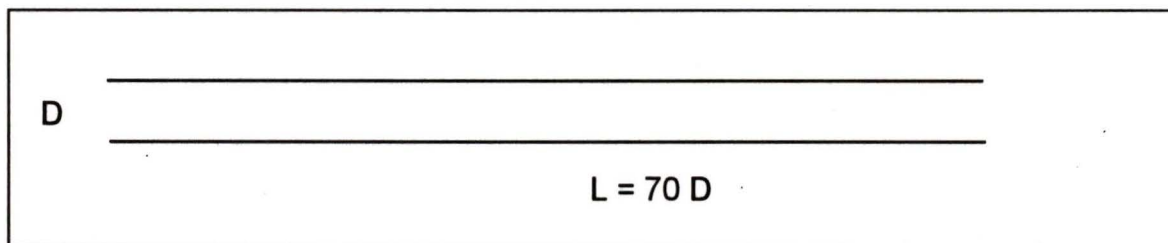


Figure 4.1: Domain Considered for 2D Simulations

4.1.2 Grid Used

The grid used to incorporate the effects of the porous section was a 3x12x3 grid inside the parallel plate duct, and a 7 point grid inside the porous region. The grid is the same as that illustrated in figure 3.5 in Chapter 3. A summary of the grid parameters is shown in the table below.

Grid	Size	Subdivisions	Geometric Ratio
Top Wall	0.01 mm	3	1.0
Main Channel	0.99 mm	12	1.9 Symmetric
Near Porous Wall	0.01 mm	3	1.0
Porous Section	0.1 mm	7	0.7

Table 4.1: Grid Parameters in the Y direction for the Two Dimensional Single Component Model

4.2 Parametric Results

The parametric results will be used to determine entrance lengths and pressure drops for the porous section ducts.

4.2.1 Pressure Drop

The pressure drop in the duct has an important relation to heat and mass transfer through the shear stress analogy. Essentially wherever shear stress is large, heat transfer and mass transfer will both also be large because the convective transport is the determining factor in heat/mass transfer capability of a flow. The greater the shear stress, the greater the velocity gradient near the wall and hence the greater ability of the flow to transport other flow scalars such as mass fractions or enthalpy. Shear stress is considered to be the sole dissipating effect within the flow (since other forms of viscous dissipation are considered negligible), and hence the shear stress is often considered as a friction factor for the duct.

4.2.2 Entrance Effects

Entrance effects are those transport phenomena, which occur only near the entrance region of a duct. The entrance region is considered to be that region where the peak velocity in the hydrodynamic centre of the duct is less than 99% of the fully developed velocity. The entrance region is characterized by higher velocity gradients near the wall and hence improved heat and mass transfer. The corollary of larger velocity gradients is an increase in the shear stress and thus pressure drop within the entrance region. These effects are present in a logarithmically decreasing state along the ducts axis. The effects are greatest at the entrance and fade rapidly as the duct length increases. While these effects are not extremely significant, they can be exploited especially when the greater goal of this work is considered. The tube cell architecture allows for customized duct lengths which would allow ducts that experience entrance effects for a very large portion of their length.

4.2.3 Friction Factor

For a 2-D duct the friction factor times Reynolds number is simply a function of the sum of the shear stress on the top and bottom boundaries of the duct as well as the local bulk velocity.

Hence

$$Cf = \frac{(\tau_t + \tau_b)D_h}{\mu \bar{u}} \quad (36)$$

where \bar{u} is the average or bulk velocity, τ_t is the shear stress on the top wall and τ_b is the shear stress on the bottom interface.

Several different cases were run to consider the effects of injection (flow into the porous section from the environment outside the model) and suction (flow out of the porous section to the environment outside the model) velocity on the friction factor and entrance length of the single phase flow. For laminar flow the friction coefficient Cf is always inversely proportional to Reynolds number so that $CfRe$ should be constant for fully developed flow. The graph below show the effect of varying the injection velocity from $2.072E-4$ up to $2.072E0$. These velocities correspond to a fractional injection velocity from 0.001 % up to 10%, or a wall Reynolds number (Re_w) or 0.01 to 100.

4.2.4 Injection Results

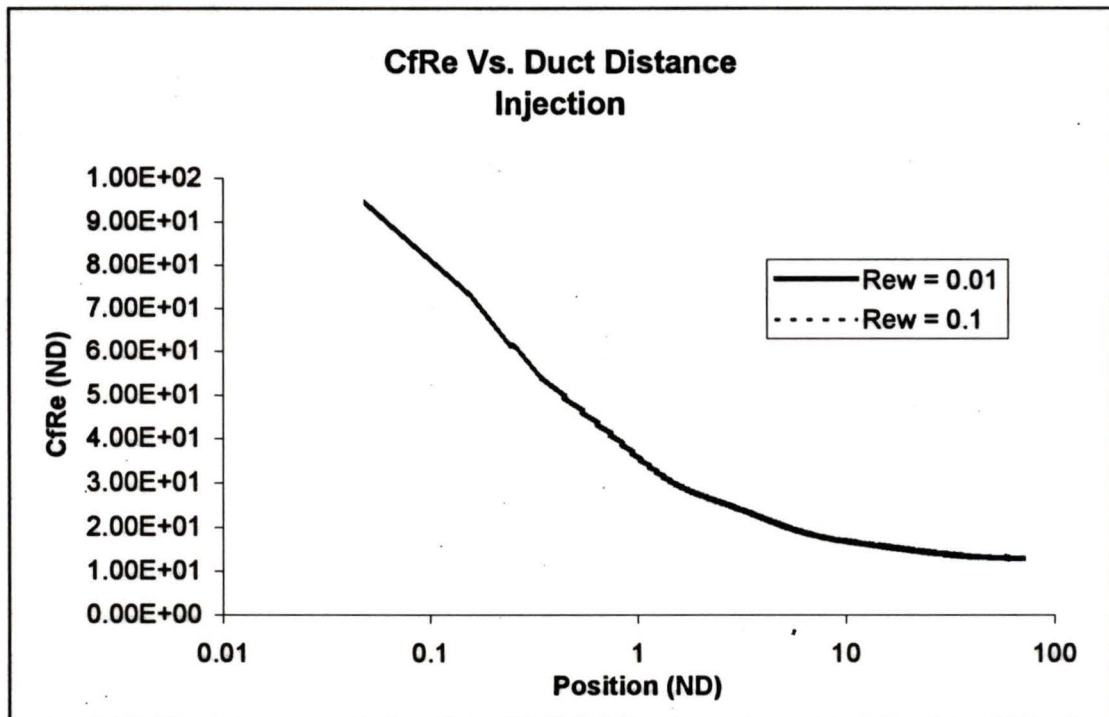


Figure 4.2: Friction Factor Results for 2D Case with Injection. The Reynolds number is 1000, and Re_w is the wall Reynolds number.

The results are very consistent with expectations as Cheng found that injection increased the friction factor, while suction decreased the friction factor. This effect can be explained quite simply by the fact that the injection pushes the velocity maxima towards the opposite side of the duct, thereby decreasing the velocity gradient in the vicinity of the porous wall. The shear stress decreases in proportion with the velocity gradient decrease. Near the non-porous wall on the opposite side of the duct, the peak velocity is moved closer to the wall, but more significantly it is moved away from the porous wall. The result is another slight

increase in the shear along the non-porous wall, which is greater in absolute value than the decrease at the porous well. The sum of the two effects is a slightly increased friction factor.

4.2.5 Suction Results

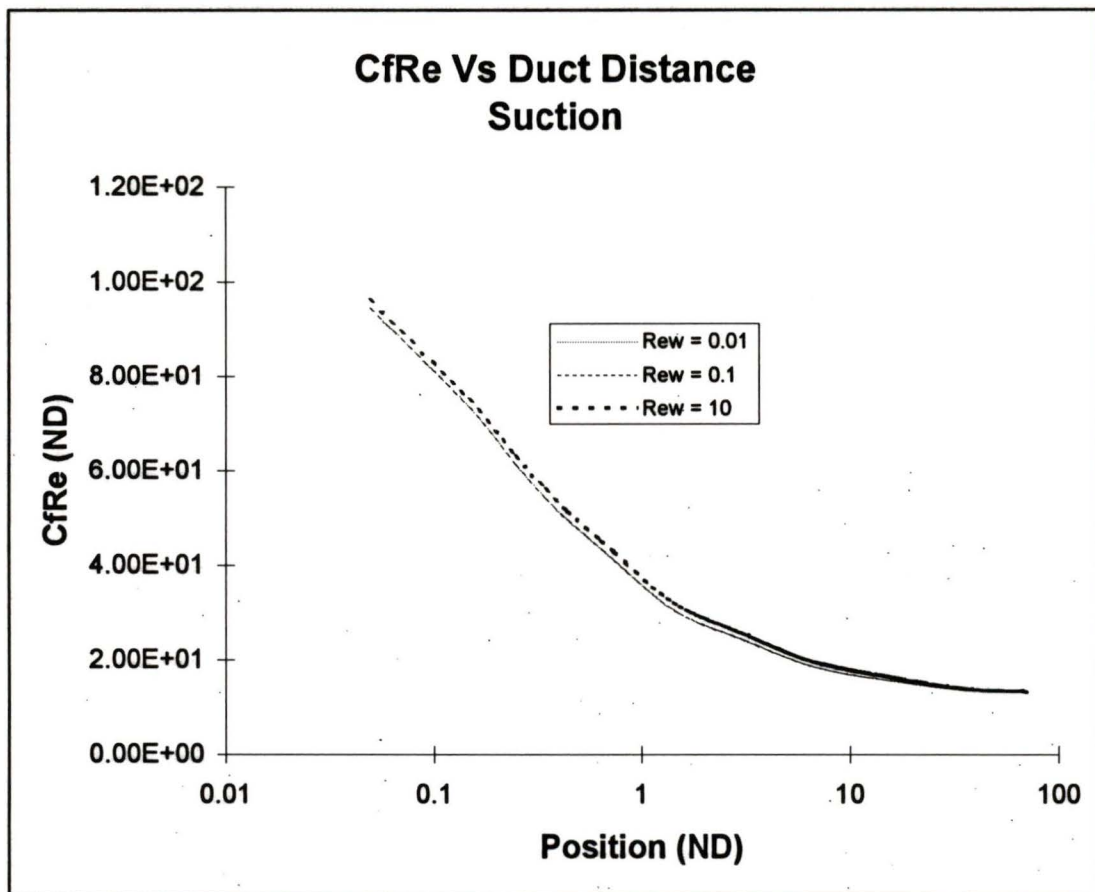


Figure 4.3: Friction Factor Results for 2D Case with Suction

For the suction case, the higher wall Reynolds number leads to an increase in the development length and hence the friction factor appears to be greater for the developing part of the flow. In a complementary fashion to the injection flow,

the velocity maxima is skewed towards the porous section and the friction factor decreases.

4.2.6 Entrance Length

The entrance length for a porous walled duct is a somewhat difficult point to define. For an injection flow it is defined as the velocity profiles are within 1% of being similar. This quasi-developed state can also be identified from the friction factor graph as the point at which the curve becomes level. The friction factor approaches a constant value indicating a similar velocity profile for the rest of the ducts length. For suction flow it is somewhat more complicated. Suction flow by its nature can not develop forever along the duct, because suction implies that at some point, all the inlet mass at the duct's entrance will be removed through the wall. Secondly, at sufficiently high suction rates, the phenomena of flow reversal may occur at the porous wall and similarity profiles cannot be maintain under such conditions. For suction flow entrance length is just defined as the point where the friction factor approaches within 99% of the temporarily constant value. For both injection and suction, the entrance length is approximately 20 times the hydraulic diameter for a Reynolds number of 1000. Since laminar flow is known to have a linear relationship between Reynolds number and entrance length, this leads to

$$\text{Re}L_e = 0.02 \quad (37)$$

for the porous sectioned 2-D duct.

4.3 Three Dimensional Results

A three dimensional model was used to investigate the effects of a square duct on the velocity distributions inside the duct. The porous section model was extended to three dimensions so that all the previously identified phenomena would be present in the 3-D model. The permeable wall model was not extended to three dimensions because it lacked several of the important features of the porous section model.

4.3.1 Domain Considered

It was necessary to even further restrict the domain considered in the three dimensional simulation because the computer memory requirements expand both with the increased grid size in the third direction, and with the addition of another momentum equation to solve for. The domain was reduced to 30 times the hydraulic diameter of the duct. The following figure illustrates the domain.

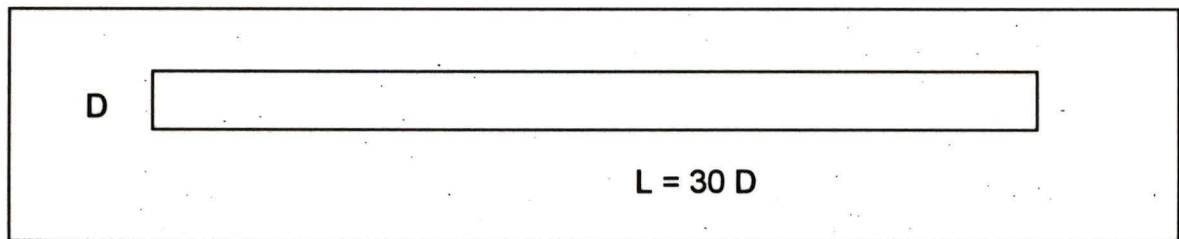


Figure 4.4: Domain Considered for Three Dimensional Square Duct

4.3.2 Grid Used

The grid used for the 3-D simulations was a straightforward extension of the 2-D grid. It featured the same spacing in the X-direction, but reduced the total length simulated to 30mm or 30 hydraulic diameters. The new Z direction was covered with 10 grid points with a smaller geometric ratio than that used in the Y direction for the main part of the duct. The following figure illustrates the grid in the Y and Z directions. The complete Y and Z grid statistics are tabulated below the figure.

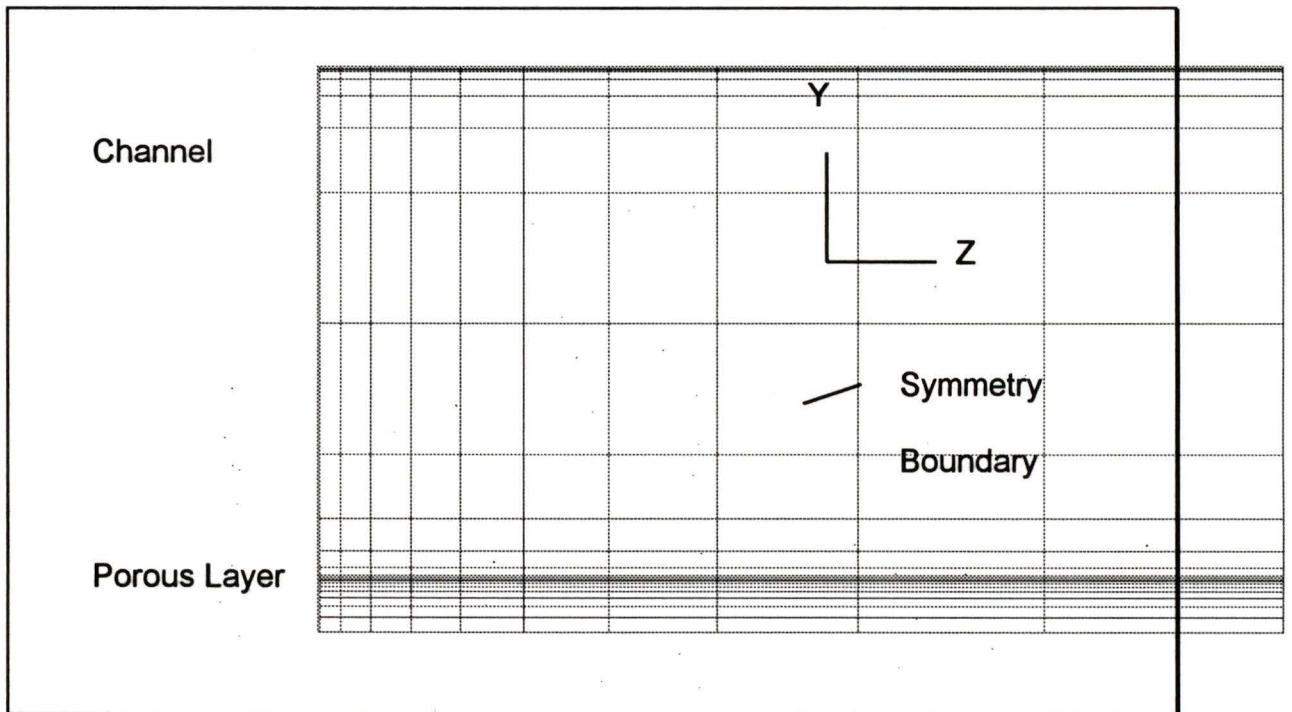


Figure 4.5: Three dimensional square grid viewed from the X direction

Grid	Size	Subdivisions	Geometric Ratio
Top Wall -Y	0.01 mm	3	1.0
Main Channel - Y	0.99 mm	12	1.9 Symmetric
Near Porous Wall - Y	0.01 mm	3	1.0
Porous Section - Y	0.1 mm	7	0.7
Transverse Direction - Z	1.0 mm	9	1.2

Table 4.2: Grid Summary in the Y and Z directions for the Three Dimensional Single Component Model

4.3.3 Injection Results

The friction factor was treated in a similar fashion to the 2-D case and plotted on a logarithmic duct axis graph shown below. Fewer parametric cases were considered because the 2-D results had indicated where the variation would likely occur and thus where to focus computational effort.

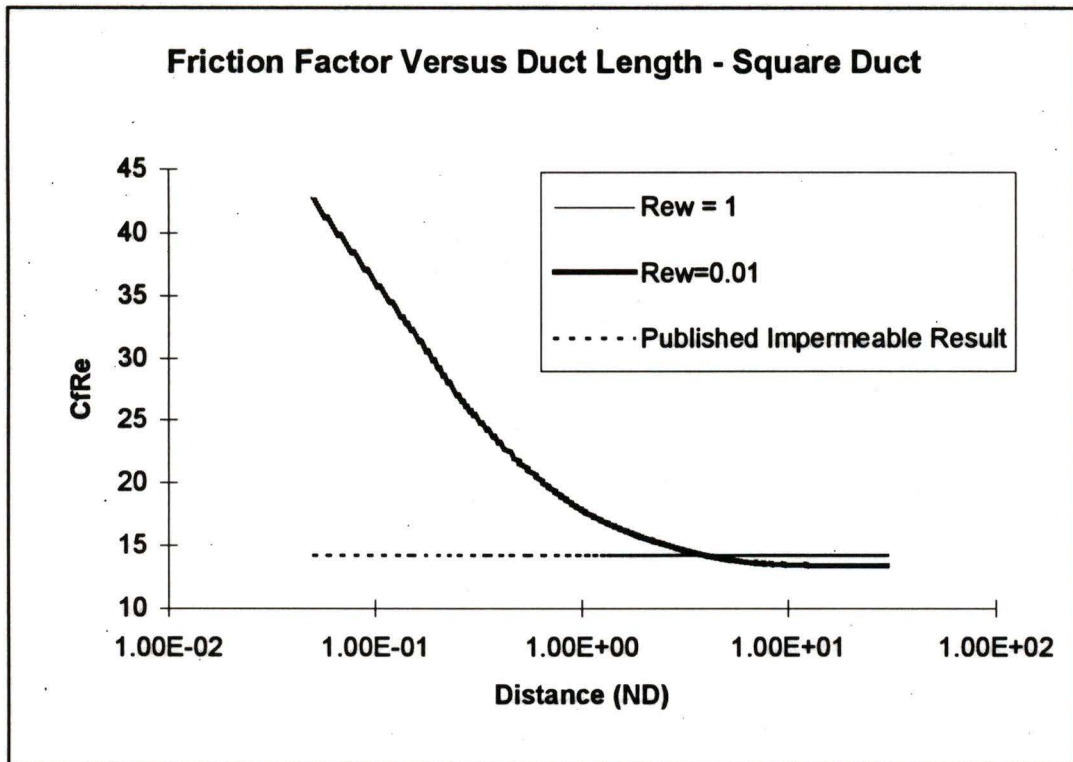


Figure 4.6: Three Dimensional Friction Factors: Injection

The injection results are similar to the 2D results for injection. The friction factor for both a 1% and 0.01% injection flow show a slightly smaller than impermeable friction factor when fully developed. Injection is expected to increase the friction factor slightly, however, the increase reported in Cheng's correlation is only 2% for a Re_w of 1. The present model predicts a decrease of 5% and yields the same trends with Reynolds number. The greater the injection Reynolds number, the greater the fully developed friction factor.

4.3.4 Suction Results

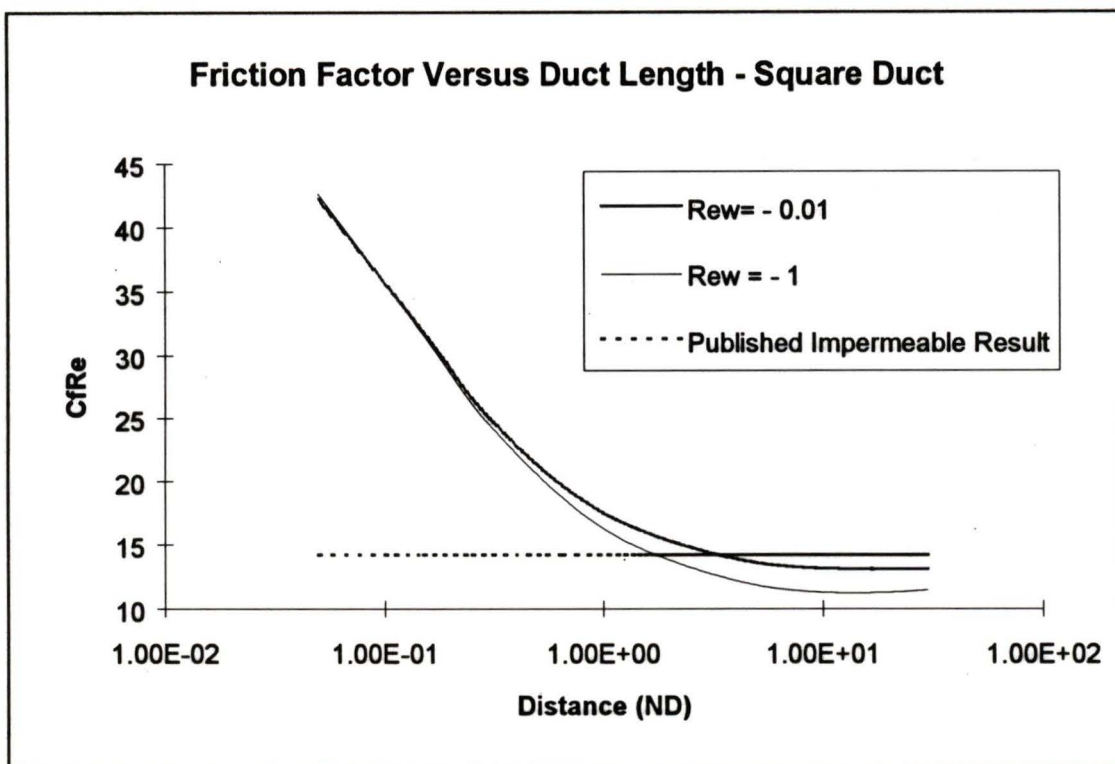


Figure 4.7: Friction Factors for Three Dimensional Case with Suction

The suction results indicate the smaller friction factor caused by the skewing of the hydrodynamic centre towards the porous section. The difference between the suction rate of $Re_w = -1$ and $Re_w = -0.01$ is more pronounced with the suction case than the injection case. This is caused by the rapidly decreasing bulk velocity for the high suction case. The overall effect of reduced friction factors with respect to the Cheng correlation can be explained by three factors. First the porous section model of this thesis utilizes a non-zero slip velocity at the porous interface, which will create a smaller friction factor. Secondly, the grid utilized by this thesis is coarser than the grid used by Cheng. Cheng

utilized a 41X41 grid in the cross stream directions, while this model utilizes a 18X20 grid. From the validation results in chapter 2,(see Figure 2.3) the friction factor tends to be under predicted by a coarse grid. Finally, the Cheng model utilizes a simplified set of equations compared to the more complete set implemented in CFX. Overall, the friction factors were predicted within 8% of the Cheng correlation.

Chapter 5 Multi Component Model

The final stage in this project was to create a multi component model that would be used to simulate the concentration distributions throughout the duct and attached porous section. The multi component flow was modeled with a mass fraction equation.

5.1 Mass Fraction Equation

The CFX code has the capability of solving a general scalar transport equation that allows the user to solve for concentrations or mass fractions of two or more species in a given fluid. The momentum and continuity equations for the whole fluid remain the same. The concentration is treated as a scalar to be solved for after the velocity distribution has been determined from the solution of the continuity and momentum equations.

5.2 Modification Details

There are a number of modifications that have been performed to CFX in order to permit the modeling of the more complex boundary conditions present in the porous duct. The most critical modification was the slip velocity correction, but additional modifications have been made to the mass fraction equation. These have mostly been modifications to the internal code, but some of the boundary modifications are add-on extensions to the code.

5.2.1 Mass Fraction Boundary Conditions

The boundary conditions available within CFX allow for a specification of a mass fraction at a boundary. A specified flux is not permitted. The result of having a specified mass fraction, which is an uncoupled scalar equation, is that the mass fraction can diffuse across an outlet. If the specified mass fraction is not the correct physical value that would exist at the outlet, this diffusion results in an additional non-physical diffusion. The diffusion is of the same order of magnitude as the velocities at the porous section outlet because the specified velocities at the outlet are caused by the diffusion of the chemical reactant to the catalyst layer. In short, the inner domain mass fraction distribution is very sensitive to the outlet mass fraction. It is desirable for this project to determine what the mass fraction distribution is throughout the flow domain and not have this distribution influenced by the exit conditions.

5.2.2 Sources and Sinks

The options available through the command file for sources and sinks are limited to a specified sink over a given region of the porous section. The sink can be a function of the local value of the mass fractions, or a fixed value. For the problem considered, the removal of mass fraction is expected to vary with the location within the duct so a fixed value is not appropriate. Furthermore the

destruction of the mass fraction is not dependent on the local value of the mass fraction, but rather on the gradient of the mass fraction, through the diffusivity of the two component system. Therefore it was not possible to utilize the readily available sinks in the command file, but rather an appropriately varying sink was specified through FORTRAN programming.

5.2.3 A Natural Mass Fraction Boundary Condition

The mass fraction distribution is not dependent on the outlet conditions, but the solution is sensitive to the specified outlet conditions. To remove the sensitivity, the logical course is to utilize information from inside the domain to specify an appropriate mass fraction at the boundary. Numerically, the simplest possible solution is to utilize an upwind approach.

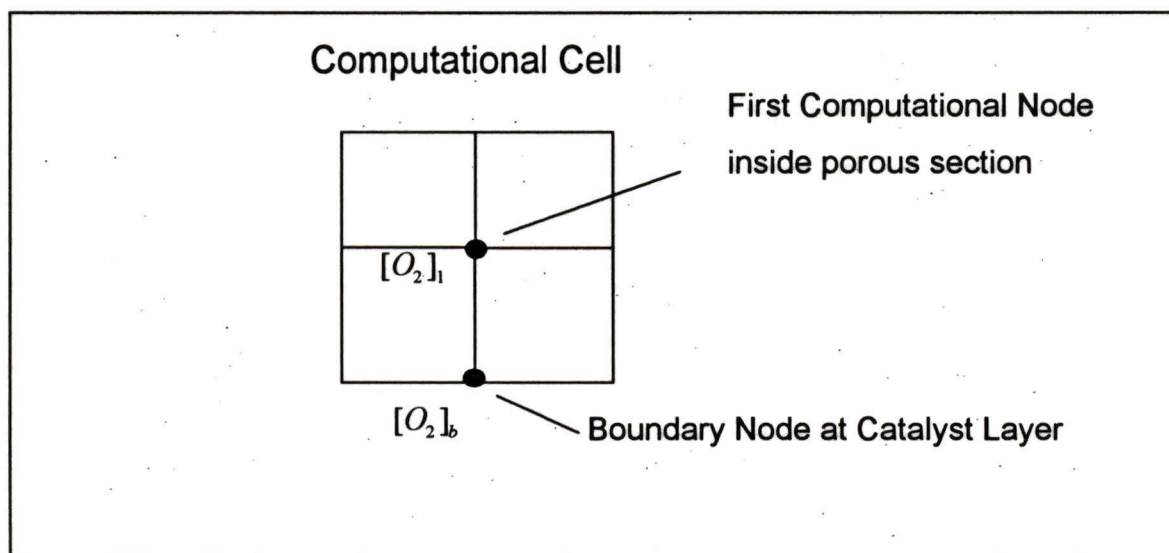


Figure 5.1: Upwind Boundary conditions at the porous section

The upwind approach leads to

$$[o_2]_b = [o_2]_i \quad (38)$$

where $[o_2]_b$ is the mass fraction at the boundary, and $[o_2]_i$ is the mass fraction just inside the domain. The mass fraction at the boundary will be updated every iteration and set equal to the mass fraction of the first computational cell inside the porous section. The boundary condition has now become a function of conditions inside the porous section, and more importantly, the problem of undesirable artificial diffusion has been solved. Since there is no gradient across the outlet, there can be no diffusion of the mass fraction. The possibility of a convergence related problem due to the explicit nature of the boundary conditions was identified, however, no difficulties were encountered when the velocity boundary condition is fixed. The passive scalar nature of the mass fraction equation means that the solutions of the momentum and continuity equations, which are the most demanding for the solver, are not affected, whereas the scalar is solved rapidly by the efficient solver within CFX.

5.2.4 Sink Options

In the real problem that this model represents, there is a chemical reaction at the boundary of the porous section, which involves only one component of the combined fluid. The mass fraction boundary utilized by default in CFX results in

a mass flow through the outlet boundary, which contains only a portion of the oxygen consumed in the reaction. The additional mass flow is of the non-consumed component, which would be nitrogen for a cathode side channel. To compensate for the additional oxygen, which would be consumed if the mixture leaving the duct were entirely composed of oxygen, a sink must be used. This sink is simply the mass flow rate that leaves the domain multiplied by the difference between the mass fraction that leaves the domain and a mass fraction equal to 1, which corresponds to a pure fluid. Returning to figure 5.1, the sink is specified at the first computational point inside the domain.

$$Sink = \rho V_{out} (1 - [O_2]) \quad (39)$$

5.2.4.1 Verification of Sink Term

In order to validate the new sink term, the CFX default conditions were compared with the new modified sink term. The oxygen concentration profiles are illustrated in the following figure.

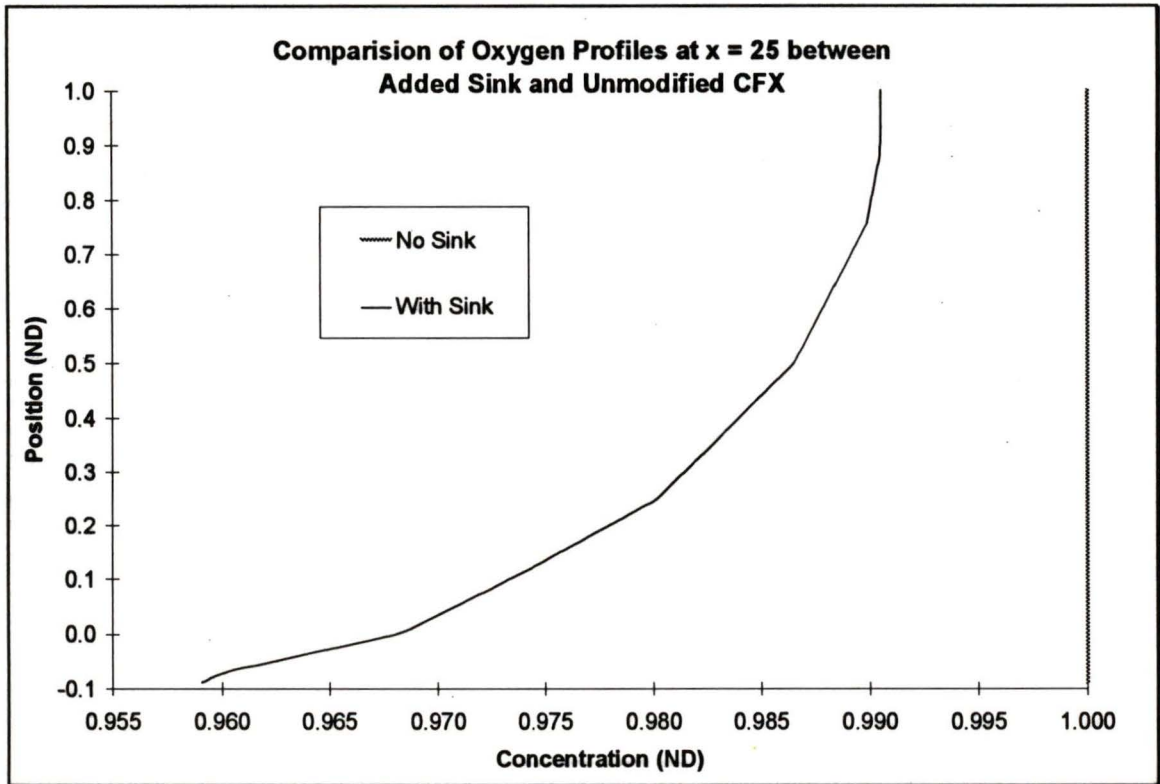


Figure 5.2 Comparison of oxygen profiles under CFX default and with modified sink term. The concentration has been non-dimensionalized by the inlet concentration of 0.2.

As can be readily seen in the figure, the CFX default predicts the concentration of oxygen to be constant across the entire channel. Furthermore there has been no depletion of oxygen relative to its initial concentration as evidenced by the constant value of 1 ND. The modified sink term predicts a parabolic profile to the oxygen concentration and also shows relative depletion of oxygen. This figure shows that a sink term is necessary to predict the reaction and transport of oxygen in the duct. To verify that the correct amount of oxygen is being depleted a balance of oxygen mass flows was conducted.

5.2.4.2 Balance of Oxygen Mass Flow

A simple balance of oxygen mass flow for a uniform current density of 1.0 A/cm^2 along the duct shows that the oxygen sink term is correctly implemented. The results are shown in the table below.

	CFX Default	Modified Sink Term
Oxygen Mass Flow In	2.080 E -7	2.080 E -7
Oxygen Mass Flow Out	2.071 E -7	2.033 E -7
Oxygen Mass Flow Required to Catalyst	4.700 E-9	4.700 E -9
Net Oxygen Flow to Catalyst	9.400 E-10	4.700 E -9

Table 5.1 Oxygen Mass Flow Balance

The comparison between the oxygen mass flow required to sustain the current density shows that the modified sink term provides the correct amount of oxygen consumption to match the oxygen utilized in the chemical reaction. The CFX default on the other hand, does not consider the destruction of oxygen beyond what leaves the duct as a component of the flow to the catalyst layer, thereby not consuming sufficient oxygen at the modeled catalyst layer.

5.2.5 Maximum Diffusion Boundary Condition

The prediction of maximum mass transport was generated by modifying the velocity boundary conditions at the catalyst layer. An implicit boundary condition

was created. The velocity out of the boundary was calculated based on an assumed Fick's law of diffusion. This assumption is valid because the highly resistive nature of the electrode ensures that the pressure inside the duct produces a very minor velocity though to the catalyst. A diagram illustrating the physical effects and the derivation of the diffusion velocity is shown below.

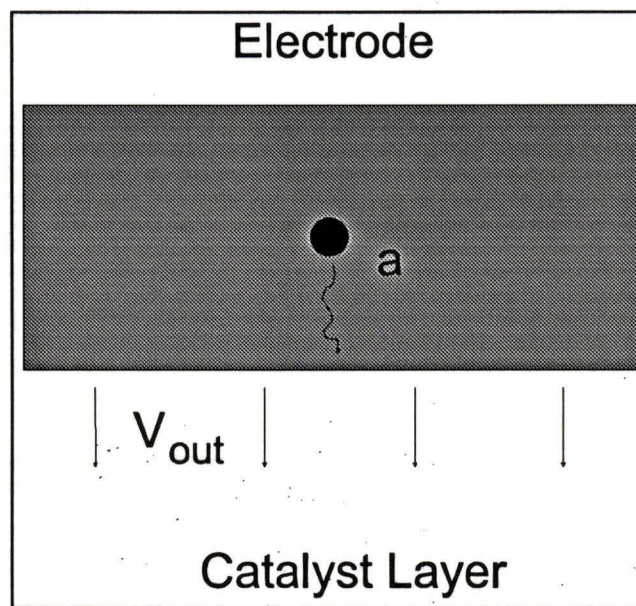


Figure 5.3: Illustration of Diffusion from the bottom of the electrode to the Catalyst layer

Fick's law of diffusion [23] is given by

$$G = -\rho D_i \nabla m \quad (40)$$

where G is the mass flux, D_i is the diffusion coefficient, and ∇m is the concentration gradient. The velocity is given by

$$V = \rho G \quad (41)$$

so using the definition of the Schmidt number we have

$$V = -\frac{\mu}{\rho Sc_i} \nabla m \quad (42)$$

Writing this as a difference equation about point a in the diagram leads to

$$V = -\frac{\mu}{\rho Sc_i} \frac{[MassFraction]_a - MassFraction_{catalyst}}{[y_a - y_{catalyst}]} \quad (43)$$

The velocity out of the porous section can now be specified based on the mass fraction equations. The coupling between the mass fraction equation and the momentum equations means that the true maximum mass transport capability of the combined system can be determined.

5.2.6 Pressure Boundary Condition

The other form of boundary condition utilized to determine the maximum mass transfer ability of the duct was a pressure boundary condition. The limiting pressure drop across the porous section is the gauge pressure of the fluid inside the duct. While incompressible flow solutions only produce a differential pressure, the absolute pressure of the fluid must still be considered when judging final results. It was observed that the maximum diffusion boundary

condition produced a pressure drop that far exceeded the operating pressure inside a fuel cell channel. The only recourse to this case is to utilize a pressure boundary condition at the catalyst layer. The pressure boundary condition is not sensitive to the internal concentration of oxygen in the duct and hence this boundary condition is more arbitrary than is desirable. It does at least maintain reasonable pressure drops within the duct.

5.3 Grid Used

The grid used for the mass fraction calculations was the same grid that was used for the single component calculations. The grid was illustrated in Figures 3.5 and 4.5 and summarized in Tables 4.1 and 4.2.

5.4 Three Dimensional Results

The results from a three dimensional square geometry are presented below in various non-dimensional forms.

5.4.1 Concentration Profiles

The following figure shows the concentration profiles at a distance of $x = 25$.

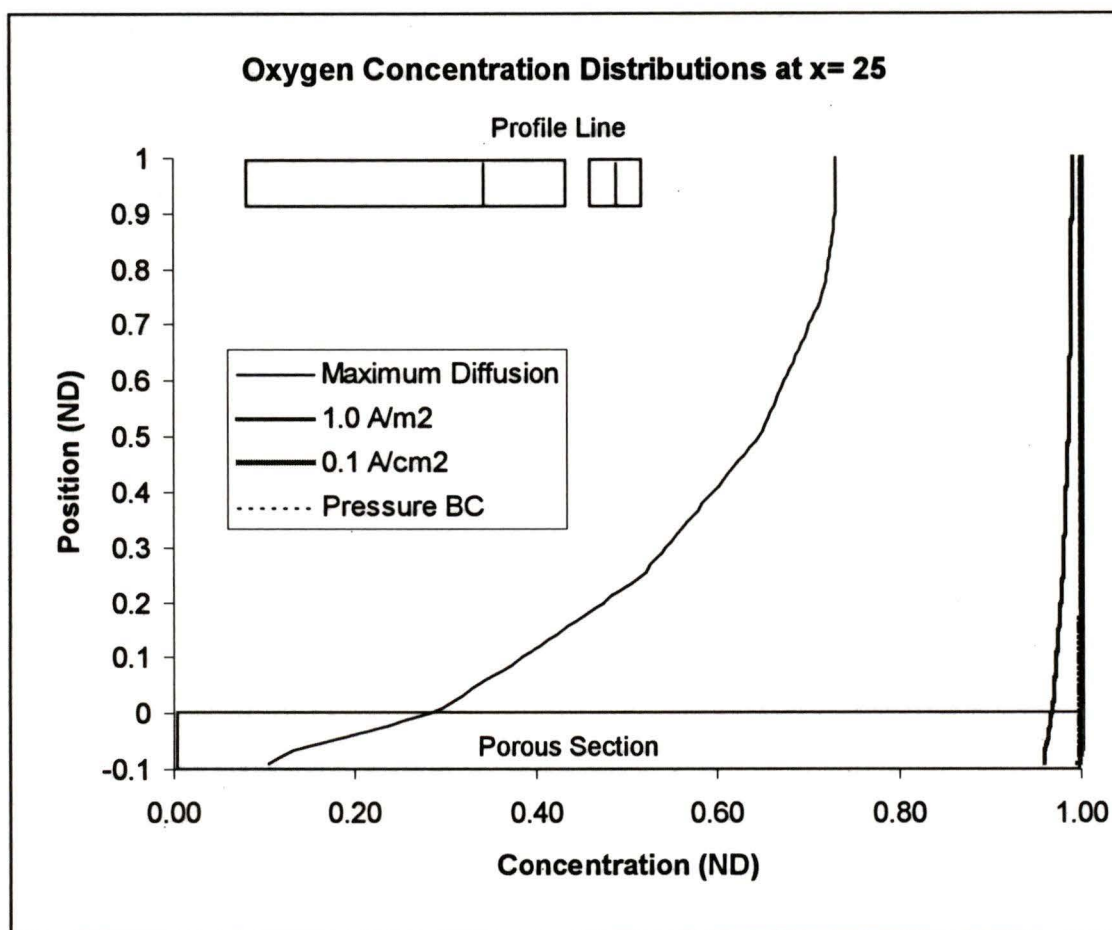


Figure 5.4: Oxygen concentration Profiles at $X = 25$. Concentration is non-dimensionalized by the inlet concentration of 0.2.

The profiles of both the nominal 100 mA/cm² case and the 1.0 A/cm² case show only a small variation across the duct. The maximum diffusion case, conversely, shows a significant variation across the duct. The distribution has no gradient in the y direction at the non-porous wall indicating a physically realistic solution.

The distribution through the rest of the duct shows a logarithmically decreasing concentration across the duct caused by the removal of oxygen at the catalyst layer. There is a clear change in the behaviour of the concentration profile at the porous interface. The profile decreases more rapidly to the catalyst layer concentration and hence the y gradient of the oxygen increases. This change is caused by the porous section accelerating the flow out of the bottom of the duct. As the concentration is inversely coupled to the velocity, the concentration must decrease as the velocity increases.

5.4.2 Oxygen Velocity at the Catalyst Velocity

The following figure shows the oxygen velocity at the catalyst velocity, non-dimensionalized by the bulk inlet velocity, along the main axis of the duct, which is non-dimensionalized by the hydraulic diameter.

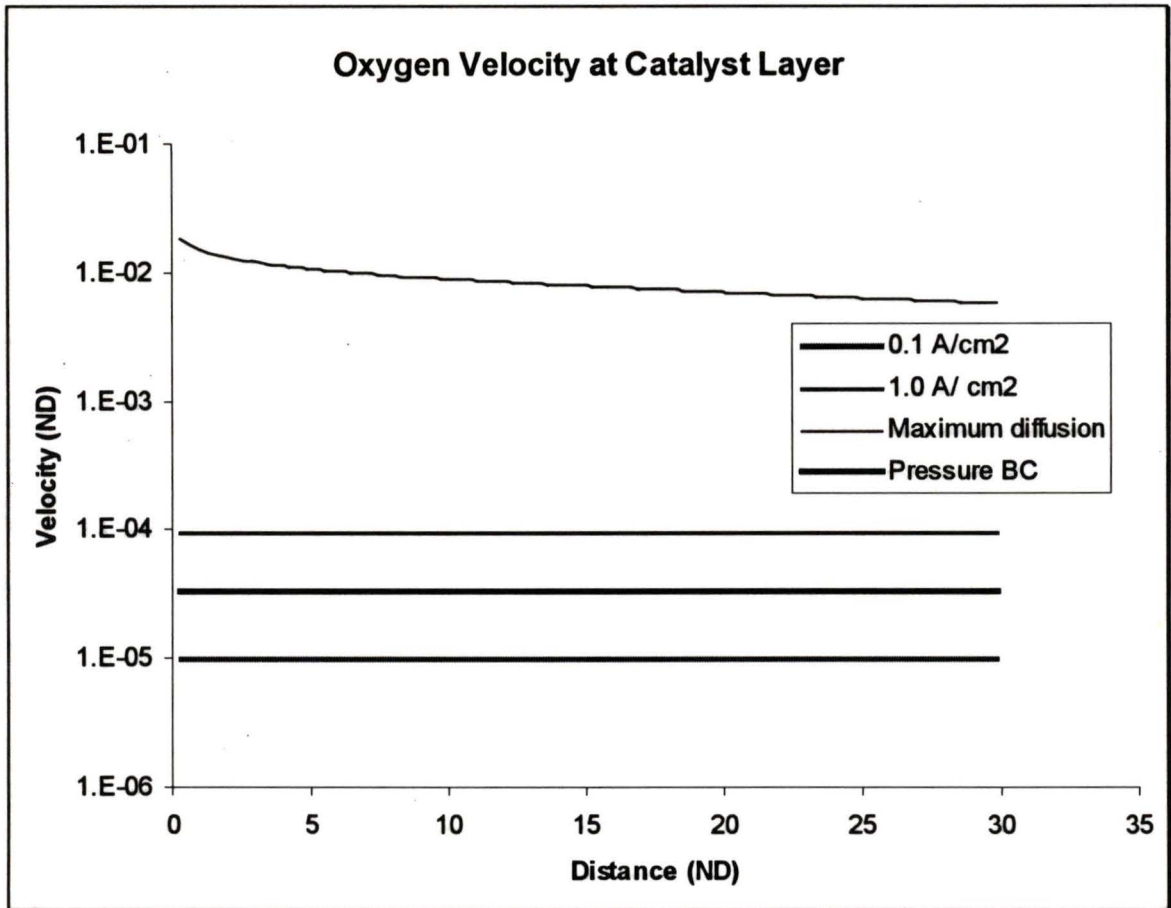


Figure 5.5: Plot of Oxygen Velocity (\propto Current Density) along the X Axis of the duct. The velocities are averaged in the Z direction.

The plot of the catalyst layer velocity along the duct reveals some interesting behaviour in the maximum diffusion case. There is a greater than exponential decay in the first 5 diameters down the duct, at which point the catalyst velocity and thus current density settles to a constant logarithmic decay as would be expected in a chemical reaction. The catalyst velocity of the two previous cases is prescribed as a constant along the boundary and hence there is no variation along the duct. The maximum diffusion case features catalyst velocities, which

are far greater than the 1.0 A/cm^2 case. This fact indicates that the mass transport ability of the square duct is far greater than the mass transport required at 1.0 A/cm^2 . Flooding and losses blamed on mass transport first occur at 1.0 A/cm^2 . These results would indicate that from a two component perspective, the mass transport would only become significant at rates of 10 A/cm^2 or greater which is outside of the presently conceivable current densities.

5.4.3 Velocity Contours

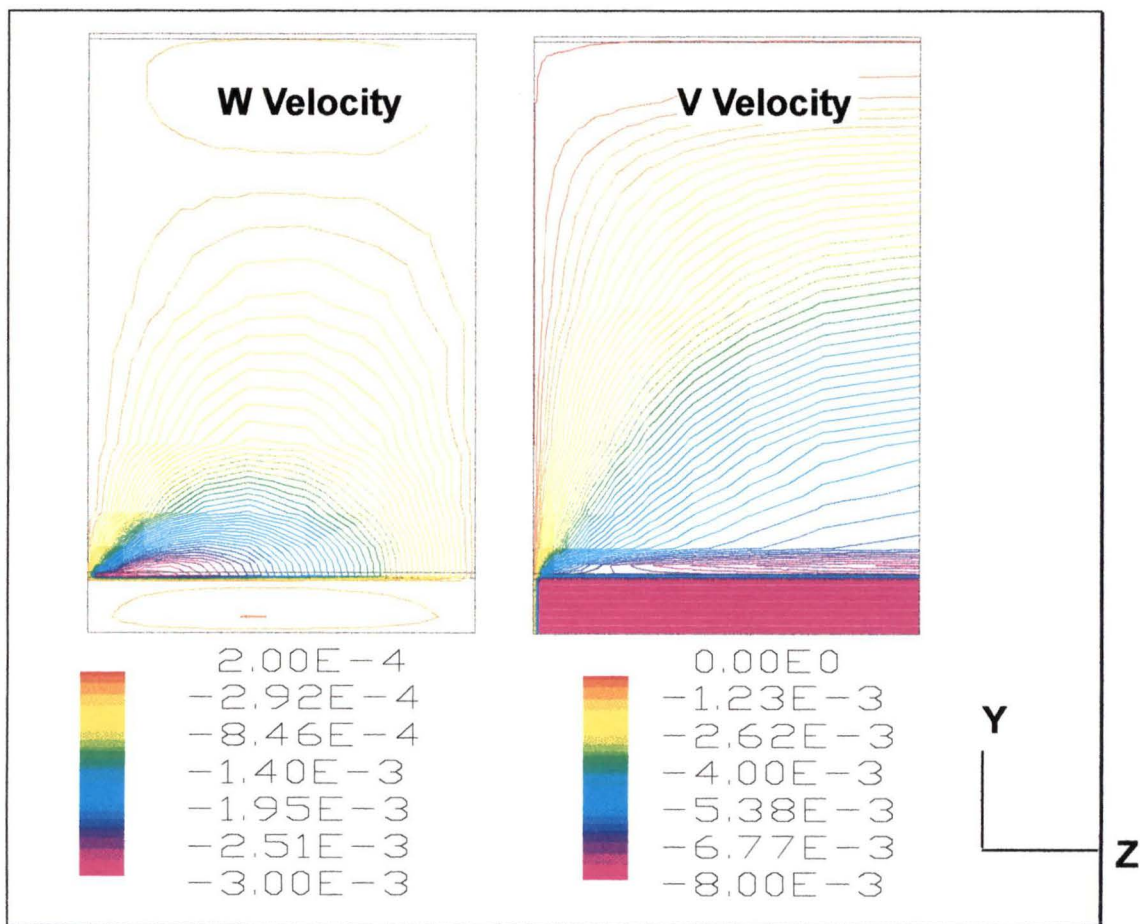


Figure 5.6: W and V Velocity contours at the X plane = 25. The constant V velocity inside the porous section has been shaded in for visibility.

The contours show how the fluid is carried by the W velocity across the porous interface towards the wall of the duct where the V velocity convects the flow into the porous section. There is no gradient of the V velocity within the porous section in the Z direction because the highly resistive porous section evenly distributes the fluid. Any local increase in the V velocity requires such a large increase in the pressure gradient that the flow is redistributed to make V constant. The W velocity shows a peak in the cross-section close to the wall where the influence of the wall slows the V velocity. The W velocity is convecting fluid into the corner in order to create that even distribution of V . The V velocity is accelerated at the interface of the porous section because the velocities plotted are the true velocities and the porous area is less than the free space area.

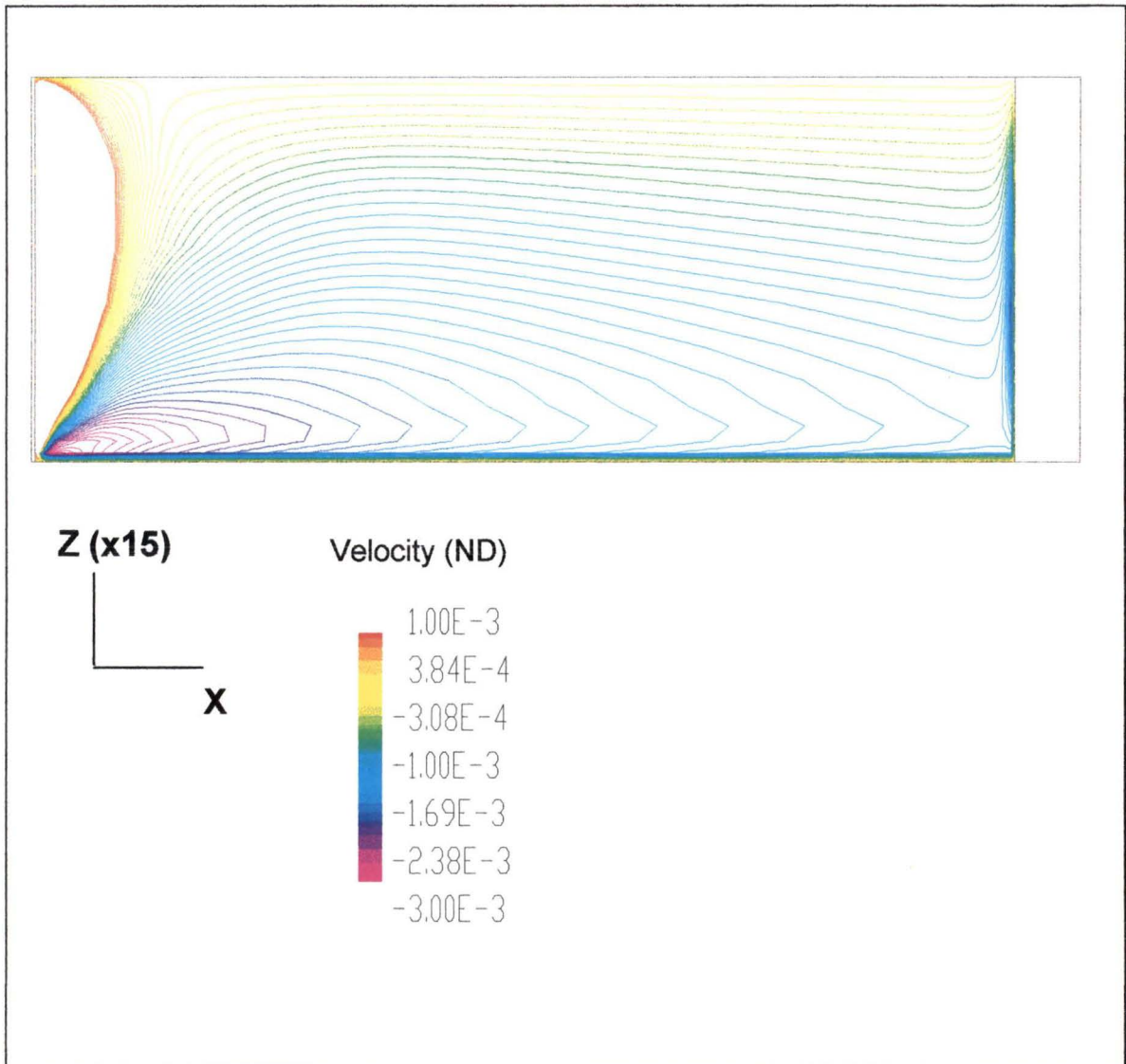


Figure 5.7: Contours of W velocity at the porous interface. The contours in the inlet region have been clipped to provide resolution over the remainder of the duct.

The above figure shows contours of the W velocity along the $y = 0$ or porous interface. The large W velocities near the wall reveal the transport of fluid towards the wall in order to evenly distribute the V velocity into the porous section. The values are greatest at the inlet where the V velocity is greatest,

and then decay in proportion to the V velocity along the X axis. The contours at the wall fall rapidly to a value of zero due to the no penetration condition at the side wall. The contours fall more softly towards the symmetry boundary because of the no flux condition at that boundary.

5.4.4 Pressure Profiles

The static pressure was plotted in the Y direction to observe how the pressure drop across the porous section is distributed. The pressure shows no variation across the duct as expected and then a linear drop through the porous section. A linear drop is expected because the highly resistive porous section produces D'Arcy flow through it, which results in a linear pressure drop. The pressure boundary condition displays a pressure drop of 4 atmospheres which was prescribed at the electrode boundary. The nominal operating case features a total pressure drop of 0.75 atmospheres which is less than $\frac{1}{4}$ of the maximum pressure drop available and hence indicates no mass transport limitations due to pressure.

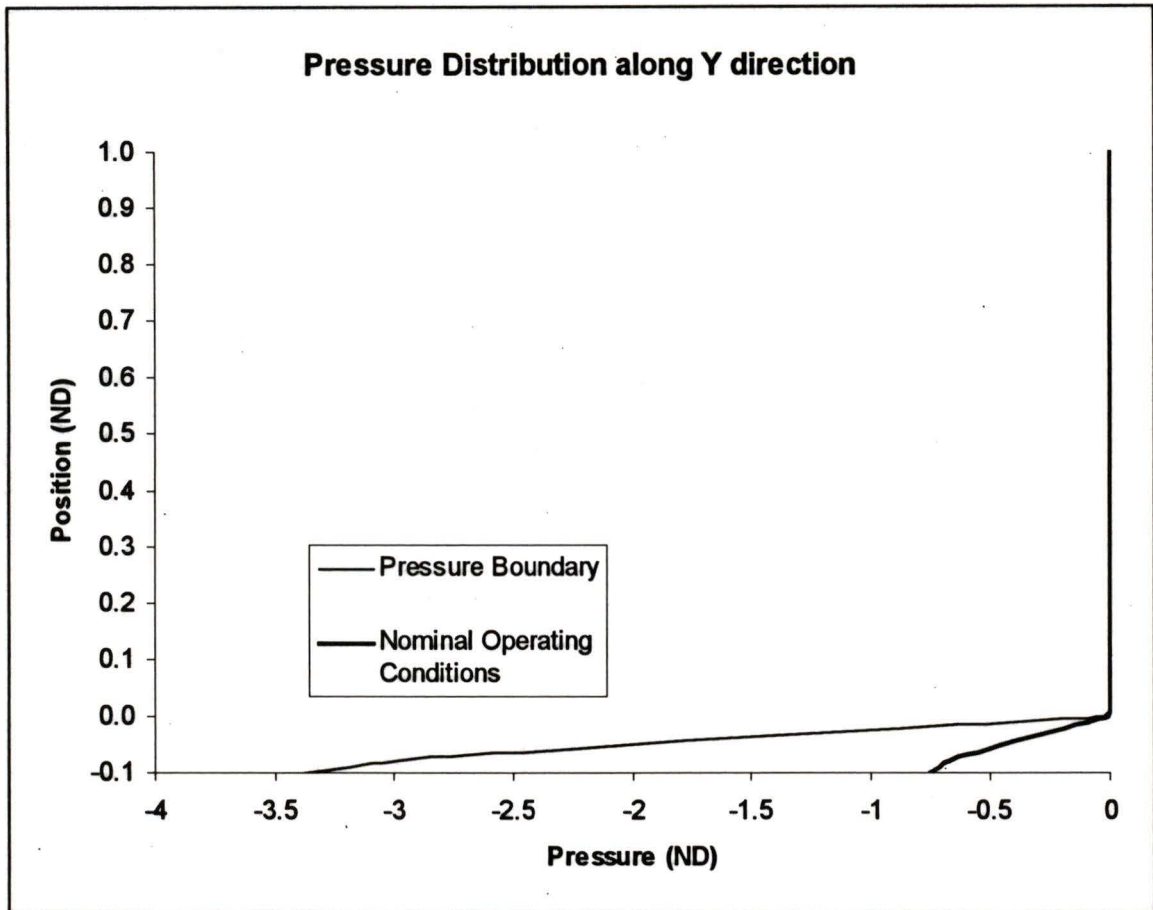


Figure 5.8: Pressure Distribution across the duct. Pressure is non-dimensionalized by one atmosphere.

The maximum diffusion case was not plotted on the same graph because it features a much greater pressure drop

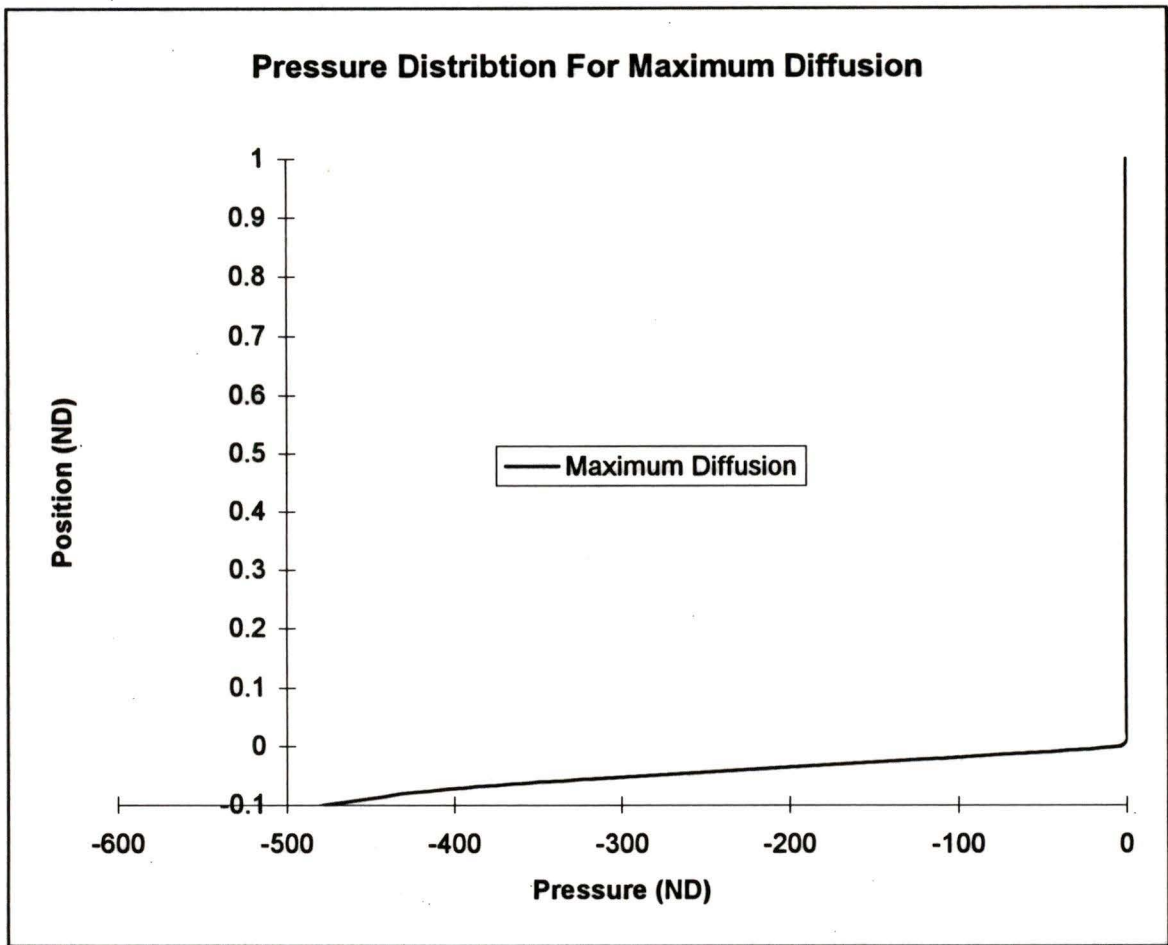


Figure 5.9: Pressure Distribution for the Maximum Diffusion Case

The pressure distribution for the maximum diffusion case features the same linear pressure drop across the porous section, but the values for the pressure drop are 100 times greater. The large velocities, which are caused by the diffusion boundary condition, are not countered by the pressure drop across the porous section because the flow is assumed to be incompressible. The constant properties combined with the incompressibility means that the pressure drop is simply with respect to a reference pressure. The model can not account for the

fact that a pressure drop of 4 atmospheres is the maximum possible pressure drop across the porous section.

5.4.5 U Velocity Development

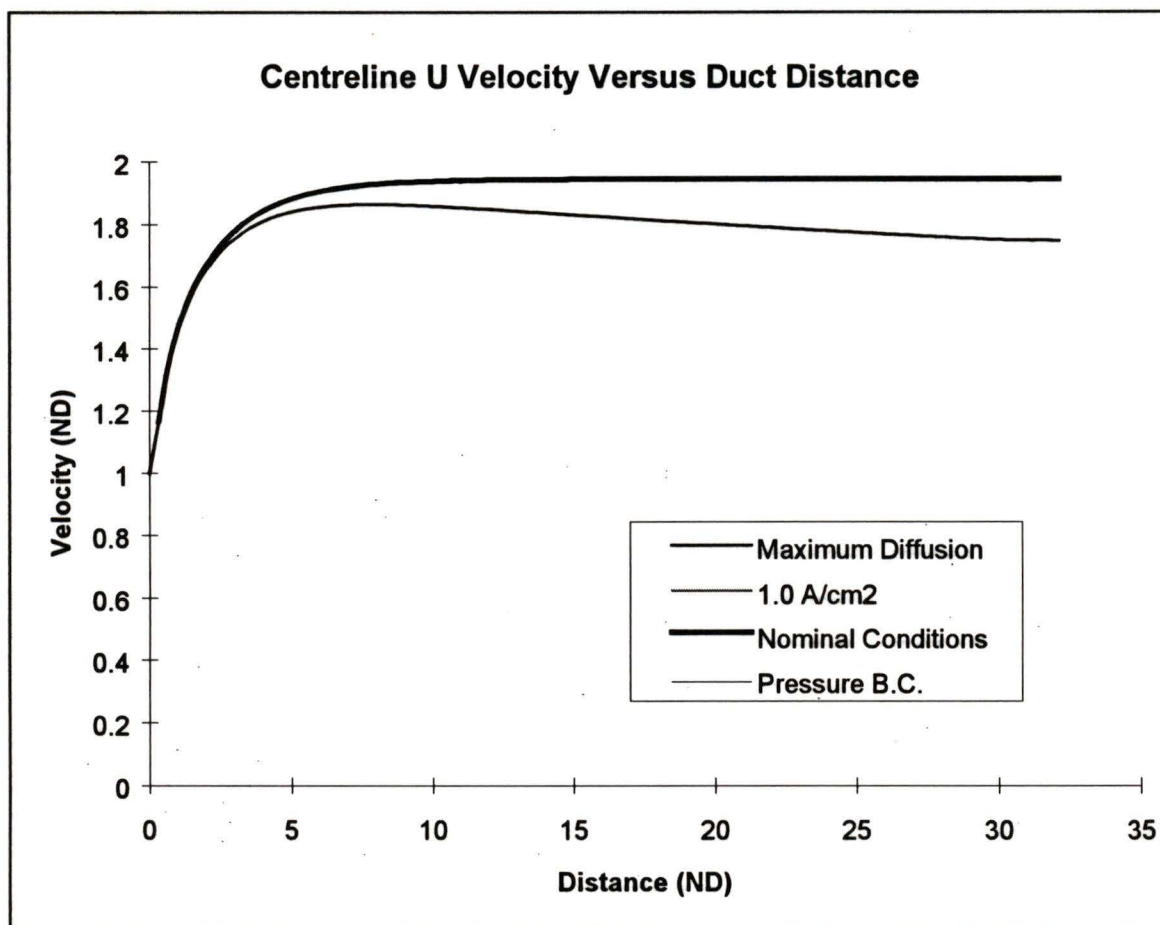


Figure 5.10: Centreline U Velocity Along the Duct. Velocity is non-dimensionalized by the inlet mean velocity.

The plot of centre line U velocity illustrates the depletion within the duct due to velocity through the catalyst layer. The maximum diffusion case is the only one

to reveal significant depletion within the domain considered by this model. The entrance length is significantly reduced by the rapid depletion of oxygen at the catalyst layer.

5.5 Resistance Effects

In a final attempt to determine the effect of the resistance on the overall solution, a small parametric study was performed on resistance. The resistance was varied while a constant pressure boundary condition was applied to the catalyst layer. The results are shown below in Figure 5.11:

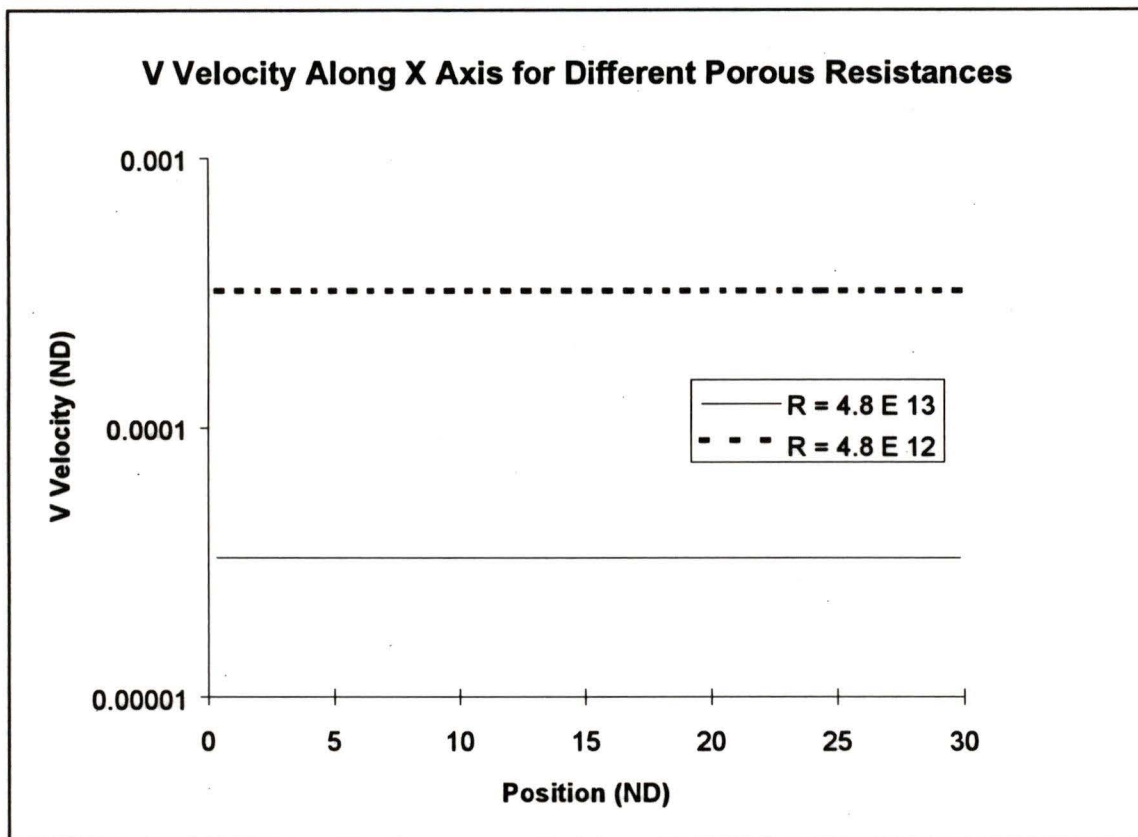


Figure 5.11: V Velocity at the Catalyst Layer along Square Duct Axis for Different Porous Section Resistances. The Catalyst Boundary Condition is constant pressure of -4 atmospheres with respect to inlet pressure.

As can be seen from the figure, the resistance is directly proportional to the V velocity through the catalyst layer and thus the mass transfer. It is therefore impossible to generate meaningful results with this model when the physical data used for the model is so uncertain. At the onset of this project it was felt that the permeability was already sufficiently small that even order or magnitude variations in it would have little effect on the flow into or through the duct. Only once the model was fully assembled was it possible to determine the effect of

varying permeability on the model and the physical problem. Various permeabilities have been used for various models in the literature.

Reference	Date	Permeability (m ²)
[13]	August 1991	3.03E-16
[12]	September 1992	4.73E-19

Table 5.2 Various electrode permeabilities used in models

The permeability varies by three orders of magnitude from one model to another. While permeability can be expected to vary from electrode to electrode, some order of magnitude boundary is needed. A physical experiment should be conducted to measure permeability of the porous material used. An accuracy of 20% would be sufficient to place greater confidence in the results created by this model.

6.0 Conclusions

The Computational Fluid Dynamics model of a fuel cell channel has lead to insight into the behaviour of the fluid reactants inside a fuel cell. A simple porous walled model was found to model some features well, but it ignored other important features. A more comprehensive model, which incorporates a porous section coupled to the channel was therefore developed.

The grid refinement study identified that heat transfer requires a more refined grid than the flow solution to generate the same level of accuracy. The grid refinement results indicate that a grid of approximately 12 grid points in each cross stream direction coupled with an appropriately sized aspect ratio in the streamwise direction produces results within 5 per cent of published results. Heat transfer computations require a 25 per cent finer grid in order to achieve the 5 per cent goal. Higher order differencing schemes were found to be of no benefit at the sufficiently refined grid utilized by this model. The insensitivity to differencing scheme is attributed to the dominance of the streamwise flow, which is aligned with the grid used and hence the flow is very well approximated by an upstream difference scheme with no significant numerical dissipation.

The validation of the present model against existing theoretical work was found to be excellent. Furthermore, the present model compared well with the numerical and experimental results of Cheng. The comparison was within 10

percent which is sufficient when considering the expected accuracy of either model and the difference between the models.

The slip velocity between a porous section and a duct is important to the velocity distribution. It is even more important to the concentration distribution within the duct when a multi-component flow is considered. The default slip velocity used by the CFX code is not correct for an arbitrary porous material so a user specified slip velocity was implemented. This specified slip velocity was based on an exact two dimensional solution for the fluid mechanics around a porous interface.

The two dimensional results for the velocity distributions revealed that the greatest pressure drop occurs across the porous section, while downstream duct pressure drops are locally insignificant. The three dimensional results indicated that the large porous section pressure drop created a uniform suction velocity distribution across the porous section. The result of this uniform velocity distribution is that duct shape is relatively unimportant in determining mass transport. The permeability of the porous section is the crucial parameter.

The mass fraction equation enabled concentration effects to be investigated from a two component perspective. The nominal operating cases created almost uniform concentration distribution across the flow stream. The diffusivity of oxygen in air is sufficient to maintain an even distribution across the duct.

For higher oxygen consumption rates, a moderate parabolic profile is maintained across the stream direction. For the maximum diffusion case, a parabolic profile is also created but this profile has a significant variation from the porous section through to the non-porous opposite wall. The variation is caused by a much greater transfer rate through the porous wall.

Overall the model provides insight into the behaviour of a two component fluid in a fuel cell environment. It also provides a good framework for coupling with the MEA model and the eventual use of a coupled model for the analysis and design of new fuel cells. The model does have some limitations caused by assumptions and the time available for the project.

6.1 Limitations of the Model and Recommendations

Numerical models have inherent approximations and limitations. In this section, the limitations of this model will be summarized. The recommendations to reduce approximations and limitations will also be mentioned.

6.1.1 Compressibility

The incompressible Navier-Stokes equations were utilized for this model. It was found that significant pressure drops occur across the carbon fibre paper or porous section, which lead to significant property variations as well as large

approximations in the nature of the equations themselves. Some attempt to compare compressible and incompressible results should be made to assess the impact of incompressibility assumptions.

6.1.2 Permeability

The permeability values used for carbon fibre paper are not well standardized between models. The pressure and thus the solution are very sensitive to the permeability value used in the model. The permeability value should be experimentally measured. A highly accurate result is not required, but an order of magnitude estimate is essential.

6.1.3 Mass Transport Capability

Based on the assumption of maximum diffusion rates at the catalyst interface, the duct is capable of providing current densities approximately ten times greater than those current densities experienced in practice. This leads to the conclusion that mass transport within the duct is not a significant factor in limiting current densities. These conclusions, however, must be drawn while recognizing the limitations of a two component, single phase model.

6.1.4 Multi-Component Flow

This model only considers two component flow. Three component flow, which occurs in the real fuel cell, is less understood and could produce effects which will further impact the concentration profiles developed within the duct. At the very least, the local concentration of water vapour will dilute the concentration of reactants as the flow stream proceeds through the fuel cell.

6.1.5 Multi-Phase Flow

This model considered only single phase flow. Multi-phase flow would have significant effects on the transport capability of the reactants through the porous layer. A liquid phase occupies pore spaces and further reduces permeability, thereby leading to greater mass transport limitations from the duct. These effects should be included through either an experimental investigation of permeability, or a more theoretical based approach that determines the reduced permeability.

Bibliography

- [1] D. M. Lu and N. Djilali, "*Heat and Species Transport in Polymer Electrolyte Membrane Fuel Cells: A Theoretical Model*", NGFT Internal Report, June 26, 1996.
- [2] S. Kakac, R. K. Shah and W. Aung, eds., **Handbook of Single-phase Convective Heat Transfer**, Chapter 3, pp 53-61, John Wiley & Sons, 1987
- [3] F. C. W. Olson, "*Flow through a pipe with a porous wall*", J. Appl. Mech., Vol 16, pp 53-54 , 1949.
- [4] A. S. Berman, "*Laminar flow in channels with porous walls*", J. Appl. Physics, Vol 27, pp 1232-1235, 1953.
- [5] G. J. Hwang, Y.C. Cheng and M. L. Ng, "*Friction factors and heat transfer in a square duct with one-walled injection and suction*", Int, J, Heat Mass Transfer, Vol 36, pp 2429-2440, 1993.
- [6] Y.C. Cheng and G.J. Hwang, "*Experimental studies of laminar flow and heat transfer in a one-porous-wall square duct with wall injection*", Int. J. Heat Mass Transfer, Vol 38, No 18, Pergamon Press.

- [7] Y.C. Cheng, **Theoretical and Experimental Study on Laminar Flow and Heat Transfer in One-Porous-Wall Ducts**, Ph. D. Dissertation, National Tsing Hua University, June 1994.
- [8] D.M. Lu and N. Djilali, "*Convective and diffusive heat and mass transport in fuel cells*", Proceedings of Canadian CFD Society Conference 1997, pp7-15 - 7-20.
- [9] J. F. Thompson, **Numerical Grid Generation: Foundations and Applications**, Elsevier Science Pub. Co., 1985.
- [10] P. M. Knupp, **Fundamentals of Grid Generation**, CRC Press, 1993.
- [11] AEA Technology, CFX Flow Solver Manual, 1996
- [12] D.M. Bernardi and M.W. Verbrugge, "*A Mathematical Model of the Solid-Polymer-Electrolyte Fuel Cell*", J. Electrochem. Soc., Vol 139, No 9, The Electrochemical Society, pp 2477-2491, September 1992.
- [13] D.M. Bernardi and M.W. Verbrugge, "*Mathematical Model of a Gas Diffusion Electrode Bonded to a Polymer Electrolyte*", AIChE Journal, Vol 37, No 8, pp 1151-1163, August 1991.

- [14] D. B. Spalding, "*A Novel Finite-Difference Formulation for Differential Expressions Involving Both First and Second Derivatives*", *Int. j. Num. Methods Eng.* Vol 4, pp 551, 1972.
- [15] S. V. Patankar, **Numerical Heat Transfer and Fluid Flow**, Chapter 5, pp 88 - 90, Taylor & Francis, 1980.
- [16] G.D. Raithby, "*A Critical Evaluation of Upstream Differencing Applied to Problems Involving Fluid Flow*", *Comp. Meth. App. Mech.*, Vol 9, pp 75-103, 1979.
- [17] B.P. Leonard, "*A Stable and Accurate Convective Modeling Procedure Based on Quadratic Upstream Interpolation*", *Comp. Meth. App. Mech.*, Vol 19, pp 59-98, 1979.
- [18] J. H. Alderton and N.S. Wilkes, "*Some Applications of New Finite Difference Schemes for Fluid Flow Problems*", AERE-R 13234, 1988.
- [19] G. S. Beavers and D. D. Joseph, "*Boundary conditions at a naturally permeable wall*", *J. Fluid Mechanics*, Vol 30, part 1, pp 197-207, 1967.
- [20] P. G. Saffman, "*On The Boundary Condition at the Surface of a Porous Medium*", *Studies in Applied Mathematics*, Vol L, No 2, MIT, pp 93-101, June 1971.

[21] N. Yucel and H. Turkoglu, "*Numerical Analysis of Fluid Flow and Mass Transfer in a Channel with a Porous Bottom Wall*", Int. J. Numerical Methods in Fluids, Vol 21, John Wiley & Sons, pp 391-399, 1995.

[22] K. Vafai and S. J. Kim, "*Fluid mechanics of the interface region between a porous medium and a fluid layer - an exact solution*", Int. J. Heat and Fluid Flow, Vol 11, No 3, Butterworth - Heinemann, pp 254 - 256, September 1990.

[23] W.M. Kays and M.E. Crawford, **Convective Heat and Mass Transfer**, McGraw -Hill, New York, 1980.

VITA

Surname: Bowers Given Names: Martin William

Place of Birth: Victoria, British Columbia, Canada

Educational Institutions Attended:

University of Victoria, 1990 - 1997

Degrees Awarded:

B.Eng. (Distinction) 1995

Honours and Awards:

NSERC Post Graduate Scholarship 1995-1997

University of Victoria President's Scholarship 1995-1997

Advanced Systems Institute Entrance Scholarship 1995

Canada Science Scholarships 1990-1995

Norman Yarrow Scholarships 1991-1995

University of Victoria Faculty of Engineering Scholarship 1992

The Woods Trust Scholarship 1992

Association of Professional Engineers of B.C. Scholarship 1991

University of Victoria Faculty of Engineering: Dean's Entrance Scholarship 1990

University of Victoria President's Entrance Scholarship 1990

B.C. Government Provincial Scholarship 1990

B.C. Ministry of Education: Passport to Education 1988 – 1990

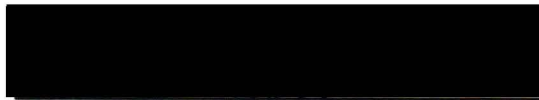
PARTIAL COPYRIGHT LICENSE

I hereby grant the right to lend my thesis to users of the University of Victoria Library, and to make single copies only for such users or in response to a request from the Library of any other university, or similar institution, on its behalf or for one of its users. I further agree that permission for extensive copying of this thesis for scholarly purposes may be granted by me or a member of the University designated by me. It is understood that copying or publication of this thesis for financial gain shall not be allowed without my written permission.

Title of Thesis:

Computational Fluid Dynamics Modeling of Flow in Fuel Cell Channels

Author



Martin William Bowers

Date

Jan 30 / 98